Schiff base functionalized silica aerogels for enhanced removal of Pb (II) and Cu (II): Performances, DFT calculations and LCA analysis

Yaoyao Zhang [a,b,c], Kangze Yuan [d,*], Luca Magagnin [c,*], Xishe Wu [b], Zhenyi Jiang [e], Wei Wang [a,b,*]

[a] Key Laboratory of Subsurface Hydrology and Ecological Effects in Arid Region of the Ministry of Education, Chang'an University, Xi'an, Shaanxi 710054, PR China
[b] School of Water and Environment, Chang'an University, Xi'an, Shaanxi 710054, PR China
[c] Department of Chemistry, Materials and Chemical Engineering "Giulio Natta", Politecnico di Milano, via Mancinelli 7, 20131 Milano, Italy
[d] College of Geological Engineering and Geomatics, Chang'an University, Xi'an, Shaanxi 710054, PR China
[e] Institute of Modern Physics, Northwest University, Xi'an, Shaanxi 710054, PR China

A B S T R A C T

Schiff base silica aerogels (SCA-X) were synthesized using amino-containing organosilanes and salicylic aldehyde as functional monomers with ethyl orthosilicate hydrolysis condensation as carrier. The influence of SCA-X on the adsorption of Pb (II) and Cu (II) under different adsorption conditions was evaluated, including the effect of solution pH, isotherm, kinetics, thermodynamics and adsorption mechanism. The batch adsorption experiments showed that SCA2 had the optimum adsorption capacity for Pb (II) (357.1 mg/g) and Cu (II) (243.9 mg/g), leading to adsorption equilibrium within 120 min and 360 min, respectively. After six adsorption–desorption cycles, SCA2 still possessed satisfactory adsorption for Pb (II) and Cu (II), demonstrating the reusability of the SCA2 adsorbent material. Kinetic studies indicated that the adsorption process could be described by a pseudo-second-order kinetic model, adsorption isotherms were in accordance with the Langmuir model, indicative of monomolecular layer adsorption. Thermodynamics evaluation revealed the nature of the adsorption process was an endothermic spontaneous process. XPS analysis combined with DFT calculations confirmed that the interaction mechanism between SCA2 and Pb (II) occurred through the coordination between the nitrogen atom donor in the Schiff base and the oxygen atom donor in the benzene ring, while the interaction between SCA2 and Cu (II) occurred mainly through the coordination between the nitrogen atom in the Schiff base and Cu (II). Life Cycle Assessment (LCA) was introduced to analyze the environmental impact of the SCA2 fabrication process and eco-friendly approaches were provided, which eventually provided theoretical evidence for the application of as-prepared material in the handling of heavy metal effluents.

1. Introduction

It is well-known that water is an irreplaceable resource on which human society depends for survival and development. In recent years, heavy metal pollution has become increasingly serious and poses a serious threat to the ecological environment [1]. Heavy metals are directly or indirectly released into water bodies through various industrial emissions, such as printing, electroplating, fertilizers, batteries, etc. [2]. Heavy metals can hardly be biodegraded and can bioaccumulate in living organisms, for example, kidney failure and Fanconi-like syndrome due to lead retention, and Wilson's disease caused by excessive copper retention [3]. Therefore, effectively eliminating heavy metal ions from water is one of the leading topics of research.

Currently, some methods available for the removal of heavy metal ions from water involve electrodialysis, adsorption, ion exchange, chemical precipitation, membrane filtration, and biological remediation [4]. In this regard, the adsorption technique has great potential for practical application over other methods thanks to its outstanding effectiveness, operational simplicity, recyclability, and cost-effectiveness [5]. The high-efficiency heavy metal removal depends largely on what adsorbent materials are used in the adsorption processes. However, conventional adsorbents exhibit unsatisfactory reusability properties as well as tunability, which has led to the development of novel, high-efficiency adsorbents [6].

The Schiff-base functionalized composites were already found to be prospective candidates for the removal of heavy metal ions from water [7]. The Schiff-based adsorbent material exhibits excellent chelation of metal ions due to its possession of azomethine (C = N) donor groups and large surface area [8]. Shahraki et al. [9] prepared Schiff base-chitosan adsorbent (MCS-ITMB) with an excellent adsorption capacity of 134.10 mg/g for Pb (II) and a high adsorption capacity after five cycles of use. Fang et al. [10] fabricated ion-imprinted Schiff base functionalized adsorbents (Cu(II)-IIPs), which exhibited a high capacity to remove Cu (II) with an adsorption capacity of 195.3 mg/g, and found that the capture of Cu (II) ions was not impacted by the presence of Ni (II), Zn (II), Cd (II), and Co (II) co-existing ions and that Cu(II)-IIP-2 possessed high stability allowing it to be recycled six times. Zhang et al. [11] synthesized a new double Schiff base chelating resin (CPS-AA), which had good reusability with adsorption capacities of 432.9 and 215.9 mg/g for Cu (II) and Pb (II), respectively. Despite the benefits of the above Schiff-based materials, they also have some drawbacks, such as adsorbent materials aggregation, which can greatly decrease their surface area and severely limit their contaminant removal properties. Therefore, the introduction of Schiff base functionalized groups into the aerogel matrix could be an excellent way to overcome this problem [12]. However, there are few relevant literature reports on the combination of Schiff base functional groups and aerogel backbones.

Available interpretations regarding the adsorption mechanism are incomplete, just including experiments, characterizations as well as classical models [13–16]. Consequently, density functional theory (DFT) has been gradually being adopted to give a more in-depth explanation of the adsorption mechanisms of pollutants by adsorbents [17,18]. DFT is an extremely useful tool, which allows theoretical computations of experiments to be solved at the atomic level [19]. In light of these factors, this study utilizes DFT calculations to explore the mechanism of adsorption involving heavy metal ions from the atomic-level point of view, which is important for explaining the elimination of Pb (II) and Cu (II) from effluents. Identifying potential trade-offs at the start of adsorbent material development can help to formulate sustainable adsorbent materials with a lower environmental impact. At an early stage of product development, the life cycle assessment of different adsorbents allows assessment of their environmental impact [20]. To identify and understand the negative environmental impacts of each product at the various stages of production, use and disposal, it is essential to assess its environmental impact at the earliest stage of development in order to avoid these impacts by changing or modifying these stages [21]. Unfortunately, the environmental impacts of Schiff-based adsorbent production are hardly to be found in the literatures.

In this work, Schiff-base functionalized aerogels (SCA-X) were fabricated by a facile sol–gel method via atmospheric pressure drying. The major aims of this work were: (1) to describe the characteristics of the fabricated Schiff base silica aerogels; (2) to evaluate the effect of different conditions on the adsorption of Pb (II) and Cu (II); (3) to uncover the atomic basis of the adsorption mechanism of Pb (II) and Cu (II) on SCA2 with DFT calculations; (4) to reveal the environmental and health effects of SCA2 preparation processes in conjunction with LCA analysis.

2. Material and methods

2.1. Materials

Tetraethoxysilane (TEOS), ethanol (EtOH), n-hexane, hydrochloric acid (HCl), ammonium hydroxide, lead chloride (PbCl$_2$), copper - chloride (CuCl$_2$), mercury dichloride (HgCl$_2$), zinc nitrate (Zn(NO$_3$)$_2$), chromic nitrate (Cr(NO$_3$)$_3$) and potassium chromate (K$_2$CrO$_4$) were supplied by Xian Chemical Reagent Co. Ltd. Salicylaldehyde (SA) and 3-aminopropyl triethoxysilane (APTES) were available from Shanghai Aladdin Biochemical Technology Co., Ltd. All chemical grades meet the experimental requirements and do not require further purification.

2.2. Preparation of Schiff-based silica aerogel adsorbents (SCA-X)

A mixture of APTES in 15 mL ethanol was slowly spiked with SA in 15 mL ethanol within 60 min under stirring. And the solution was agitated at 30 °C for 6 h, named A solution. The mixture of 10 mL TEOS, 26 mL ethanol and 12 mL 0.1 mol/L HCl solution was stirred at 60 °C for 2 h and recorded as B solution. The solution A was charged slowly into the solution B and stirred at 30 °C for 24 h. Then, 4 mL 1 mol/L ammonium hydroxide was introduced to adjust the pH to 7 ~ 8, and stirred vigorously for 5 ~ 10 min and the gel was formed after 12 h in a 40 °C water bath. The solvent exchange was then carried out 6 times with anhydrous ethanol for 6 h. Subsequently, a further solvent exchange with n-hexane was performed 4 times for 6 h. Finally, the products are dried in a vacuum drying oven at 40 °C and 60 °C for 24 h. The molar ratios of n (TEOS): n (APTES): n (SA): were 1: 0.3: 0.3, 1: 0.5: 0.5, 1: 0.7: 0.7, 1: 0.9: 0.9, respectively, and named as SCA1, SCA2, SCA3 and SCA4, respectively. SCA2 was chosen for the follow-up DFT calculations and LCA analysis as it showed the optimum adsorption properties.

2.3. Characterizations

The aerogel samples were investigated by X-ray diffraction (XRD), scanning electron microscopy (SEM), elemental analyser (EA), Fourier transform infrared spectroscopy (FTIR), Brunauer-Emmett-Teller (BET) specific surface area, thermogravimetric analysis (TGA), atomic absorption spectrophotometry (AAS) and X-ray photoelectron spectroscopy (XPS). The characterization techniques are described in detail in the Supporting Information.

2.4. Adsorption experiments

The absorption behavior of SCA-X for Pb (II) and Cu (II) was assessed in batch experiments under different conditions. Specifically, the effect of SCA-X dosage was studied on 50 mg/L of Pb (II) and 50 mg/L of Cu (II) solutions using 0.5–2.0 g/L of adsorbent in 50 mL centrifuge tubes. The effect of pH (1–6) on the adsorption of Pb (II) and Cu (II) was carried out using 1 g/L adsorbent. 0.1 M HCl and 0.1 M NaOH solutions are used to adjust the pH of the solution. For kinetic studies, adsorption was performed at 10 mg SCA2 and 10 mL of 50 mg/L Pb (II) and Cu (II) solutions with 0–240 min for Pb (II) and 0–720 min for Cu (II) at 298 K. For the absorption isotherm investigation, the initial concentrations of both Pb (II) and Cu (II) were 50–1000 mg/L at 298 K. Adsorption thermodynamic studies were conducted at different temperatures (293–318 K) with a concentration of 100 mg/L for Pb (II) and 50 mg/L for Cu (II). Six times adsorption cycling experiments were undertaken. Once the adsorption was completed every time, the saturated adsorbent was treated with 25 mL of 0.1 M HCl solution and agitated for 4 h to desorb, followed by further adsorption and desorption. It is repeated three times for each adsorption experiment and the results are obtained using the mean value. Removal efficiency (φ, %) and adsorption capacity (q, mg/g) can be obtained using Eqs. (1) and (2).

$$\varphi = \frac{c_0 - c}{c_0} \times 100\% \tag{1}$$

$$q = \frac{(c_0 - c) \times v}{w} \tag{2}$$

Where c_0 (mg•L^{-1}) and c (mg•L^{-1}) refer to concentration of Pb (II) and Cu (II) at initial and time t, respectively. v (L) relates to the solution volume and w (g) gives the adsorbent dosage.

More information regarding the kinetic, isothermal and thermodynamic models is provided in the Supporting Information.
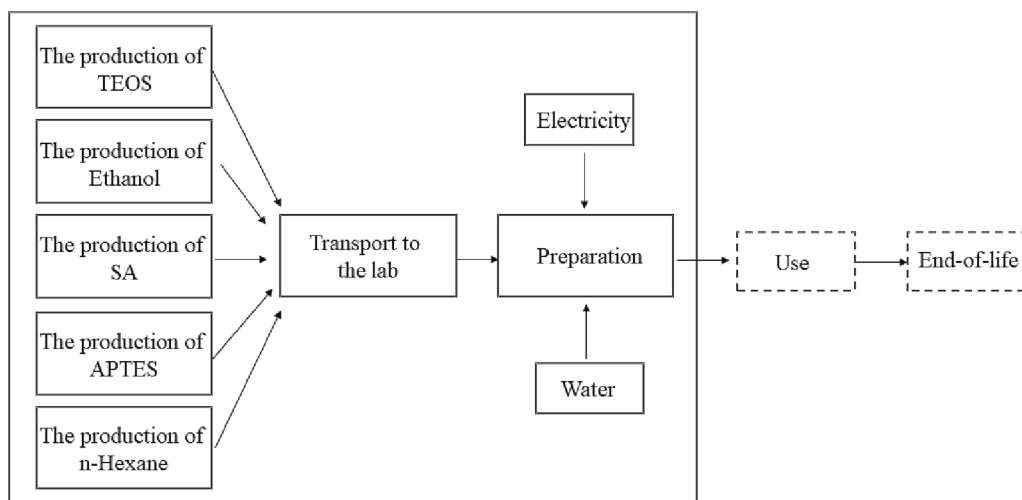
Fig. 1. Flowchart describing the SCA2 adsorbent production.

2.5. DFT calculation

The Gaussian 09 software was used for all DFT calculations [22]. Simulations have been conducted in the ground state using the B3LYP functional group [23]. Regarding geometrical optimization and frequency calculations, the LanL2DZ basis set was used for Pb and Cu atoms and the 6–31 g(d) basis set for the other atoms. The single point energy calculation employed the LanL2DZ basis set for Pb and Cu atoms and the 6–311 g(d, p) basis set for the other atoms [24]. It is calculated using an integral equation formalism polarization continuum model (IEFPCM) with water being the solvent to account for solvation effects [17]. The adsorption energy (E_{ads}) is determined as the following Eq. (3) [25].

$$E_{ads} = E_{total} - (E_{adsorbent} + E_{metal}) \qquad (3)$$

where E_{total} is the total energy of Pb (II) or Cu (II) adsorbed onto SCA2, $E_{adsorbent}$ refers the SCA2 energy and E_{metal} depicts the energy of Pb or Cu atom, respectively.

2.6. Life Cycle assessment (LCA)

2.6.1. Goal and scope definition

The goal of this study was to determine the environmental impacts associated with the production of 1 kg SCA2. While it is still at an early stage in the production process, there is a high degree of uncertainty regarding its impact on the environment, therefore, this study uses sensitivity analysis to characterize the synthesis process in order to achieve the objective of reducing environmental impact.

Life Cycle Assessment (LCA) is a useful tool for evaluating a product's environmental impact over its lifetime [26]. The use of LCA to quantify the environmental impact of SCA2 in the production process is relatively new. An environmental impact assessment was conducted using the guidelines in ISO 14044 [27]. Environmental hotspots were identified through analysis of the impact of each material used in the production of SCA2, and further environmental-friendly production strategies were developed to reduce the negative impact on sustainability. Fig. 1 provided the system boundaries for a cradle-to-grave LCA. Raw material transport distances were calculated based on China's average distance of 181 km. This work does not take into account the use and end-of-life phases, following the assumption that there is not environmental impact in use phase and the end-of-life phase does not require disposal.

2.6.2. Life cycle inventory

The second stage of LCA research is Life Cycle Inventory (LCI)

Table 1
Life Cycle Inventory for the production of 1 kg SCA2.

	Mass	Unit
Raw material input		
TEOS	0.47	kg
Ethanol	30	kg
SA	0.2	kg
APTES	0.35	kg
n-hexane	21.25	kg
Water	0.64	kg
Energy input		
Electricity	6	kWh
Transportation	181	km
Output		
SCA2	1	kg

analysis. It is responsible for collecting data about all inputs and outputs recognized at the boundaries of a system [28]. Experiments carried out in the laboratory (see section 2.2) and literatures were collected and recorded according to the boundaries mentioned above. The calculations were performed in eFootprint and the Ecoinvent database v.3.1 and CLCD were used to access all data in the Life Cycle Inventory (LCI). As a source of electricity, this study assumed that an average global mix of electricity would be used. The LCI for generating final products (SCA2) was indicated in Table 1.

2.6.3. Impact categories

The results of the LCI can be assigned to environmental issues of focus by impact category. The evaluating methodologies, including cumulative energy demand (CED), IPCC GWP 100a, and CML-IA baseline, are used. Meanwhile, seven common impact categories are investigated, namely Global Warming Potential (GWP), Acidification Potential (AP), Abiotic Depletion Potential (ADP), Eutrophication Potential (EP), Ozone Depletion Potential (ODP), Photochemical Ozone Creation Potential (POFP) and Primary Energy Demand (PED).

3. Results and discussion

3.1. Characterization

The SEM result illustrated in Fig. 2 demonstrated that the obtained samples exhibited a clear successive net-like structure with high
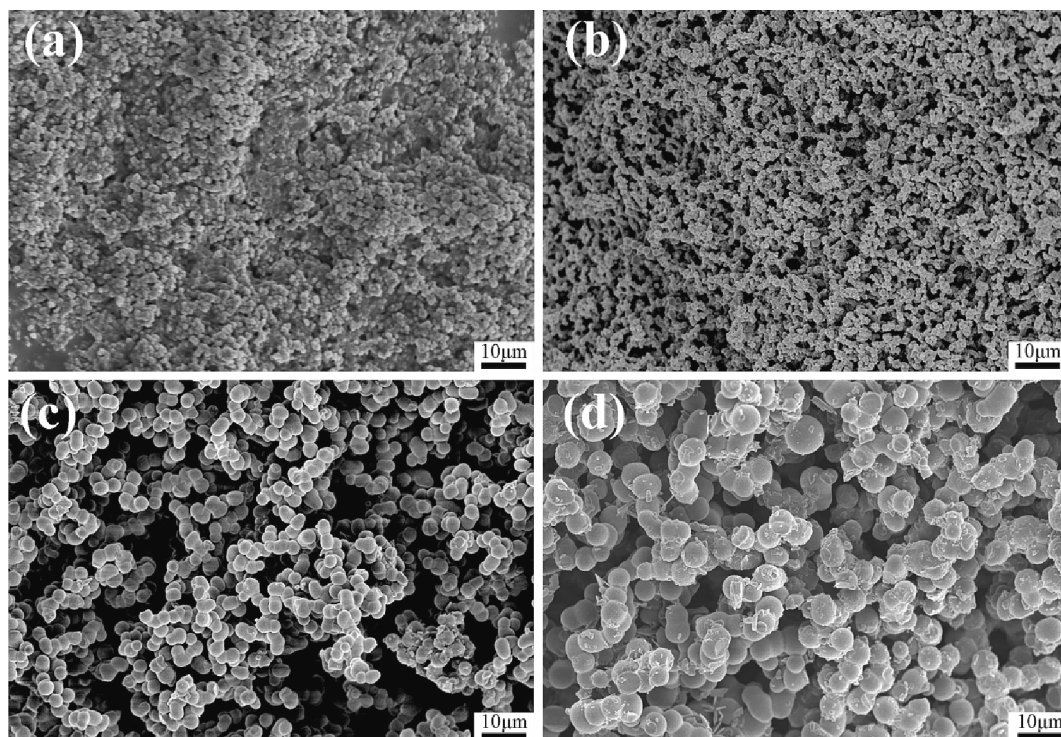
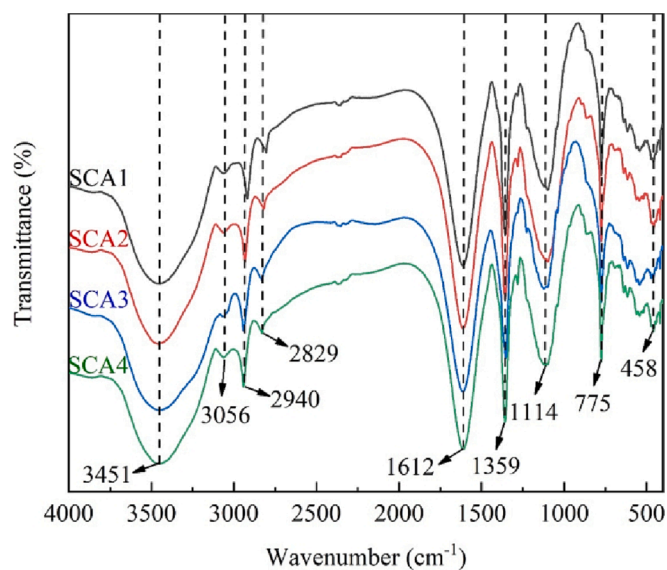**Fig. 2.** Morphology of SCA-X. (a) SCA1; (b) SCA2; (c) SCA3; (d) SCA4.

Fig. 3. FTIR spectra of SCA-X.

porosity. When the content of APTES and SA was low, a compact aerogel skeleton with a dense porous structure was formed due to the incomplete reaction (Fig. 2a). Increasing the amount of APTES and SA caused the aerogel skeleton to loosen, forming large continuous pores as secondary particles accumulate at the surface (Fig. 2b) [29]. Interesting, the aerogel skeleton surface was comparatively coarse, which facilitated the formation of a robust framework as the secondary particles were able to connect more easily. It was observed that when APTES and SA were increased further, a chains-like structure was formed with large smooth spheres (Fig. 2c and d), where phase split occurred due to the large amounts of APTES and SA [30]. Morphological images of Schiff base aerogels were displayed in Fig. S1. In addition, Table S1 presented the physical properties of Schiff base aerogels prepared with varying

amounts of APTES and SA. By increasing the amount of APTES and SA, the density and volume shrinkage of Schiff base aerogels first decreased and then increased, correspondingly the density changed from 0.35 g/cm^3 to 0.31 g/cm^3 and then increased to 0.62 g/cm^3. The volume shrinkage dropped from 17.2% to 16.6% and then increased to 24.7%, with SCA2 having the lowest density and smallest volume shrinkage. Moreover, Table S2 provided information about elemental analysis of SCA-X samples. And the C and N content of the SCA1, SCA2, SCA3 and SCA4 progressively increased with increasing APTES and SA content. It appeared that Schiff base content in samples was directly related to the amount of APTES and SA, thus the preparation of SCA-X materials was confirmed to be successful.

An investigation of the FTIR spectra was carried out for the determination of the chemical compositions of SCA-X samples (Fig. 3). The bands at 1114, 775 and 458 cm^{-1} were classified as the Si-O-Si asymmetric vibration, symmetric vibration and bending vibration [31]. The peak at 1359 cm^{-1} was assigned to a C-N stretching vibration [8]. The peaks at 2829 and 2940 cm^{-1} were ascribed to C-H asymmetric and symmetric vibration [32]. The weak peak at 3056 cm^{-1} was attributed to hydrogen vibrations on the benzene ring [33]. The broad peak at 3451 cm^{-1} was classified as the O-H stretching vibration. Additionally, a peak at 1612 cm^{-1} appeared due to the multi-bond stretching vibrations of C = N, and C = C in aromatic rings coupled with O-H from adsorbed water [10,33].

The XRD patterns of SCA-X were exhibited in Fig. S2. In all SCA-X samples, XRD patterns displayed a similar broadening peak at 2θ ≈ 21.75°, which was consistent with an amorphous structure of silica [34]. The intensity of the peaks decreased slightly with increasing APTES and SA content. According to the XRD plots, the SCA-X samples still maintained the original amorphous structure of the silica aerogel and were essentially unchanged.

A representation of N$_2$ adsorption–desorption isotherms and distributions of pore sizes was shown in Fig. 4. A type IV isotherm was found in SCA-X samples and an H3 hysteresis loop was detected, which indicated the mesoporous materials [35]. The SCA-X sample structure had an uneven distribution of pore structures, with the majority of holes
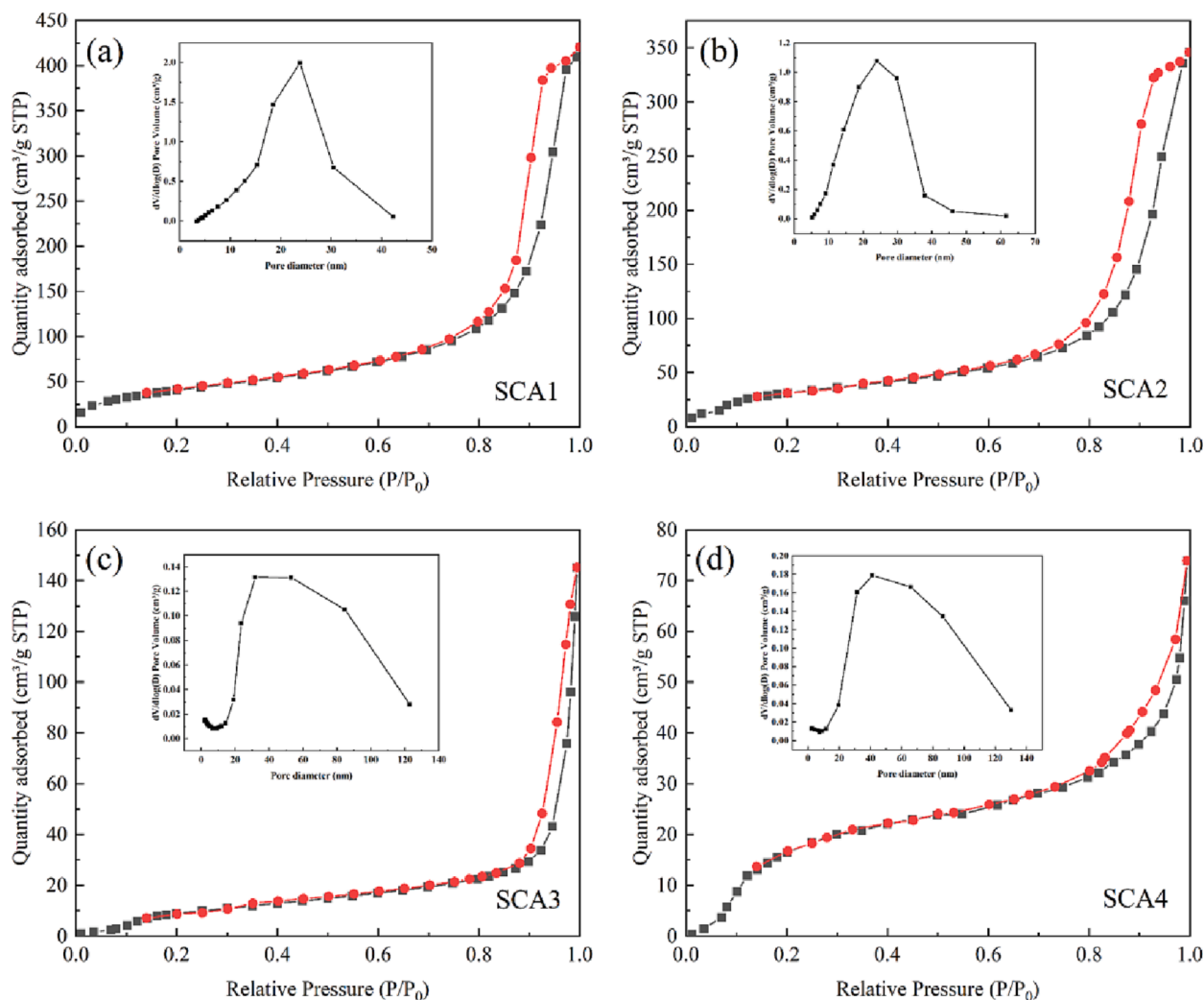
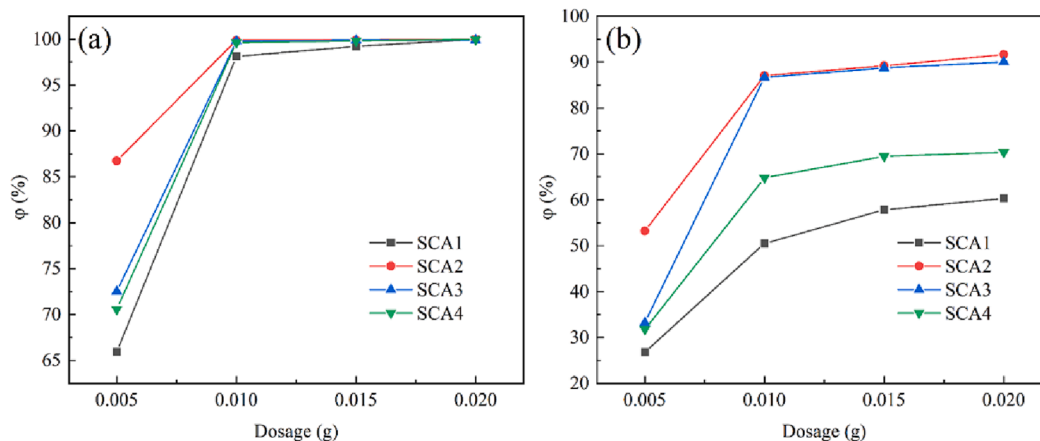**Fig. 4.** N$_2$ adsorption–desorption isotherms of SCA-X.

Fig. 5. The comparison of removal efficiencies for Pb (II) (a) and Cu (II) (b) with different adsorbents.

being of a fractured shape and flask-shaped holes with open ends [29]. The samples exhibited dramatic N$_2$ absorption around P/P$_0$ ∼ 1, demonstrating that the macroporous structures presented in SCA-X [36]. The specific surface area (SSA) of SCA1, SCA2, SCA3 and SCA4 were 152.47, 80.85, 34.87 and 17.41 m^2/g, respectively. A gradual increase in pore size of 15.78, 18.79, 22.10 and 31.06 nm can be found for SCA1,

SCA2, SCA3 and SCA4, respectively. There was a reduction in SSA due to an increased molecular volume formed when more aminosilane coupling agents and salicylic aldehydes were combined [37].

The thermogravimetric curves for the SCA-X samples were shown in **Fig. S3**. The slight weight loss of approximately 4% under 200 °C was considered to the humidity and physically adsorbed water [8]. Then, a
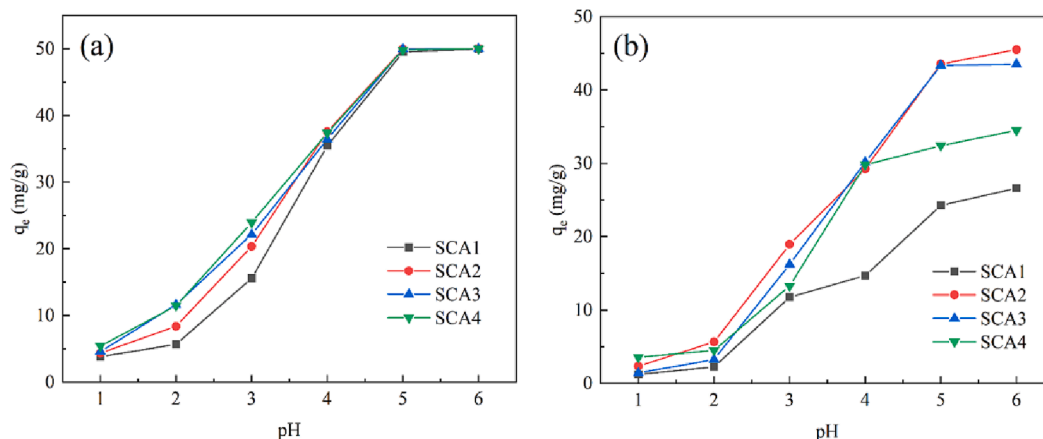
Fig. 6. The effect of pH on the Pb (II) (a) and Cu (II) (b) adsorption by SCA-X.

dramatic drop was noted between 200 and 700 °C owing to the condensation of residual silanol groups and the decomposition of Schiff bases [38]. The weight loss above 700 °C was possibly caused by the breaking of the benzene ring and the breakage of the siloxane groups of the SCA-X aerogels [39]. The final mass losses were 33.65%, 36.20%, 46.68% and 49.49% for SCA1, SCA2, SCA3 and SCA4, indicating that the increase of weight loss correspond to the increasing amount of APTES and SA.

3.2. Adsorption properties

3.2.1. Comparison of the adsorbent capacity
Fig. 5 showed the effect of aerogels obtained using different contents

of APTES and SA on the adsorption of Pb (II) and Cu (II). The SCA2 (n (TEOS): n (APTES): n (SA) = 1:0.5:0.5) adsorbent had optimal removal performance for both Pb (II) and Cu (II). As the content of APTES and SA increased, the longer macromolecular chains were generated by the reaction of APTES and SA, the increased potential resistance hindered further grafting onto the silica aerogel skeleton, and caused the aerogel particles to become larger and the SSA to decrease significantly, thus influencing the removal of heavy metals. Elemental analysis showed that a further increase in the content of APTES and SA could increase the Schiff base content, but the reduced SSA could result in part of the Schiff base being unavailable. Therefore, considering the economic benefits and adsorption performance, SCA2 was selected for the following studies on heavy metal ion adsorption [40]. In addition, the removal
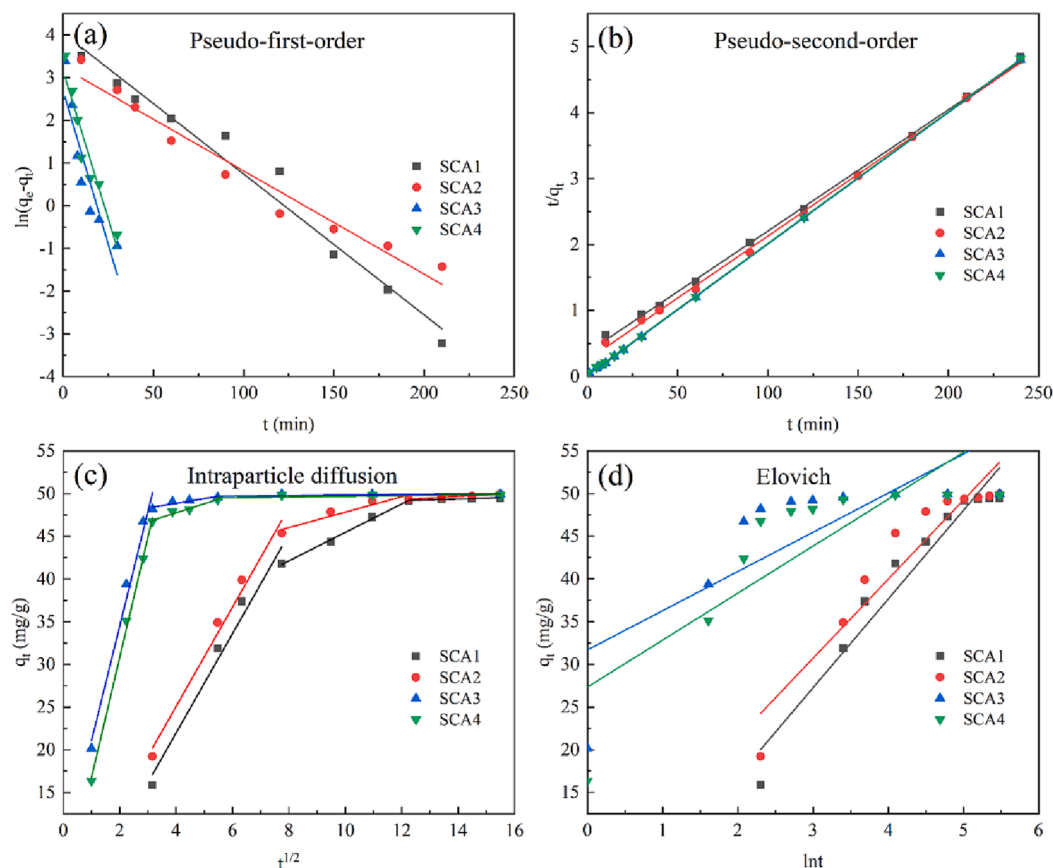

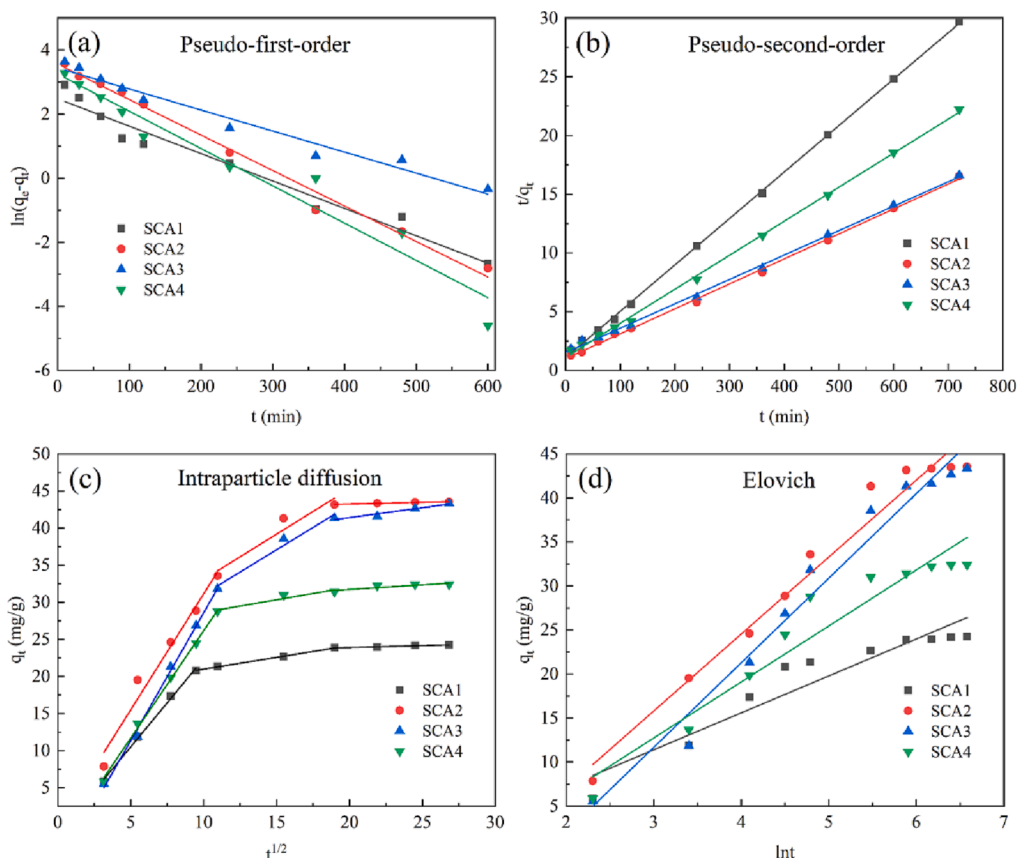**Fig. 7.** Adsorption kinetic fitting curve for Pb (II) on SCA-X.

Fig. 8. Adsorption kinetics fitting curve for Cu (II) on SCA-X.

rates of Pb (II) and Cu (II) were observed to be almost maximum at an adsorbent dosage of 0.01 g (i.e. 1 g/L), and the increase of the adsorbent dosage was not significant for improving the removal rate, so the adsorbent dosage of 1 g/L at the inflection point was chosen.

3.2.2. The effect of pH

Solution pH has a significant impact on the surface charge of adsorbents, and this will eventually influence the adsorption process [41]. Fig. 6 showed the influence of solution pH on the adsorption of Pb (II) and Cu (II) by the SCA-X adsorbents. An increase in the pH in the range 1 to 6 caused to an increase in the adsorption of Pb (II) and Cu (II) by SCA-X. Adsorption was commonly regarded as a competition between Lewis acid (Pb^{2+}, Cu^{2+}, H_3O^+) and Lewis base (-N = CH–). In solutions with a low pH (pH < 4) containing abundant H_3O^+, SCA-X surface had a lot of active sites taken up by H_3O^+ and produced protonated groups (–CH = NH^+-), leading to a low adsorption performance. Higher pH promoted Pb (II) and Cu (II) trapping on SCA-X, as the greatly reduced H_3O^+ in aqueous solution and the deprotonation of the ligand [42]. At solutions pH above 6.0, insoluble hydroxide precipitation was favored, which could lead to inaccurate test results [43]. In addition, the zeta potential analysis of SCA2 was illustrated in Fig. S4. The potential value of SCA2 dropped with rising pH. The isoelectric point of SCA2 was approximately at pH 4.28. The surface of SCA2 became protonated and positively charged when pH was below the isoelectric point, repelling positively charged metal ions in solution and hindering Pb (II) and Cu (II) adsorption. The functional groups protonated of SCA2 became

Table 2
Adsorption kinetic parameters for Pb (II) and Cu (II) on SCA-X.

| Kinetic models	Parameters	Pb (II)				Cu (II)			
		SCA1	SCA2	SCA3	SCA4	SCA1	SCA2	SCA3	SCA4
Pseudo-first-order	k_1 (min^{-1})	0.033	0.024	0.144	0.138	0.009	0.011	0.006	0.011
	q_e (mg/g)	57.03	25.41	14.83	23.61	11.94	35.21	31.25	25.90
	R^2	0.9745	0.9625	0.8333	0.9163	0.9624	0.9899	0.9694	0.9541
Pseudo-second-order	k_2 (g/(mg·min))	0.0009	0.0014	0.0305	0.0179	0.001	0.0004	0.0002	0.0007
	q_e (mg/g)	54.35	53.19	50.25	50.00	25.25	46.94	48.08	34.48
	R^2	0.9989	0.9989	1	0.9999	0.9996	0.9987	0.9984	0.9989
Elovich	α (mg/(mg·min))	7.122	12.694	4571.67	790.17	3.165	2.653	1.611	2.346
	β (mg/g)	0.096	0.108	0.218	0.182	0.238	0.114	0.104	0.157
	R^2	0.9437	0.8962	0.6150	0.6886	0.9017	0.9682	0.9717	0.9287
Intraparticle diffusion	k_{p1} (mg/(g·min$^{1/2}$))	5.814	5.815	13.427	14.076	2.374	3.125	3.449	2.896
	R^2	0.9724	0.9831	0.9828	0.9976	0.9970	0.9715	0.9959	0.9977
	k_{p2} (mg/(g·min$^{1/2}$))	1.669	0.905	0.545	1.057	0.317	1.222	1.201	0.338
	R^2	0.9962	0.9133	0.8622	0.9658	0.9982	0.9314	0.9754	0.9149
	k_{p3} (mg/(g·min$^{1/2}$))	0.099	0.174	0.031	0.040	0.052	0.047	0.266	0.123
	R^2	0.9374	0.9868	0.4646	0.4645	0.9485	0.9736	0.9331	0.7845
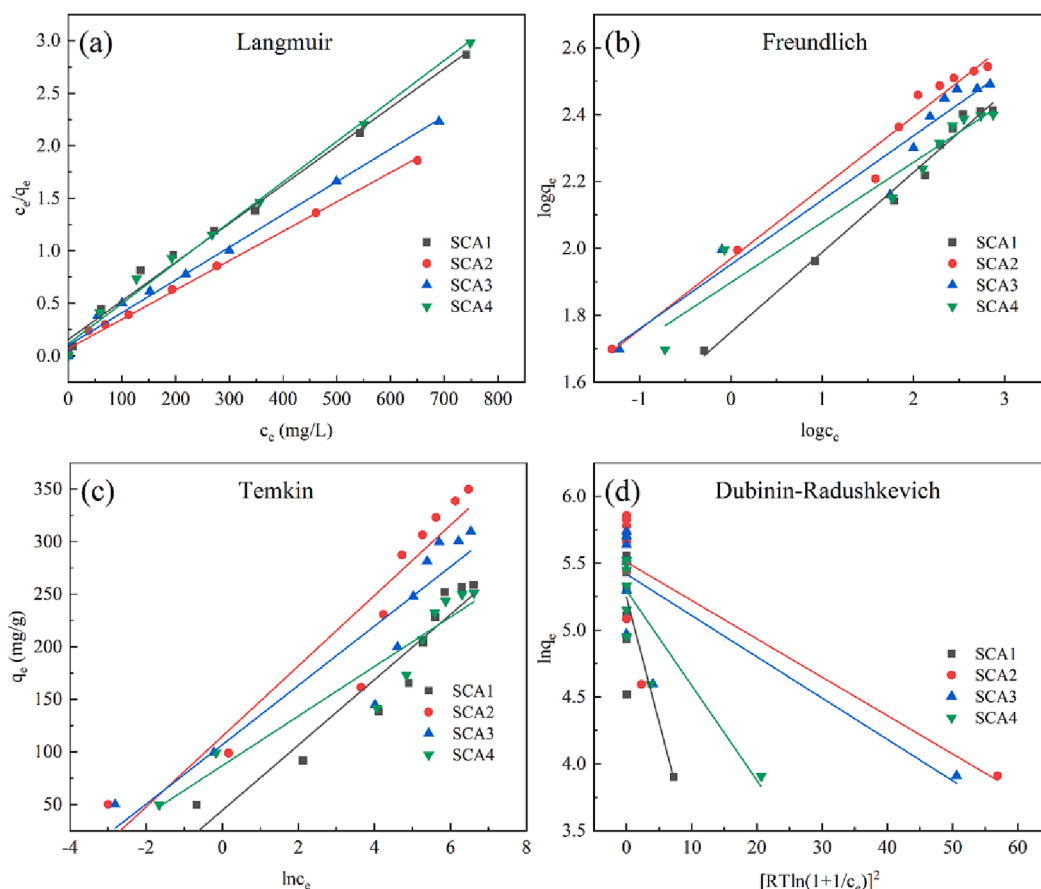
Fig. 9. Adsorption isotherm fitting curve for Pb (II) by SCA-X.

deprotonated and negatively charged when the pH was above the iso-electric point, thereby facilitating heavy metal adsorption. Thus, pH 5.0 was selected to further investigate the elimination of Pb (II) and Cu (II), considering the electrostatic attraction as mechanism for the adsorption of Pb (II) and Cu (II) [44].

3.2.3. Adsorption kinetics

The amount of adsorption increased rapidly at first, then gradually slowed down and finally reached equilibrium (**Fig. S5**). The absorption equilibrium for Pb (II) on SCA-X was eventually achieved within 120 min, while for Cu (II) at 360 min. Clearly, Pb (II) adsorption achieved adsorption equilibrium faster than Cu (II) adsorption, indicating that SCA-X adsorbents adsorbed Pb (II) more readily.

Pseudo-first-order (PFO), Pseudo-second-order (PSO), Elovich and intraparticle diffusion kinetics model were developed in order to better understand the adsorption process. The results of the fitted kinetic curves were shown in Pb (II) (Fig. 7) and Cu (II) (Fig. 8) and Table 2.

A comparison and analysis of the data in Table 2 showed that the calculated equilibrium adsorption (q_{cal}) from the PSO model (for Pb (II): 54.35, 53.19, 50.25, and 50.00 mg/g for SCA1, SCA2, SCA3, and SCA4, respectively; for Cu (II): 25.25, 46.94, 48.08, and 34.48 mg/g for SCA1, SCA2, SCA3, and SCA4, respectively) was in close accordance with the experimental equilibrium adsorption value (q_{exp}) (for Pb (II): 49.49, 49.95, 49.94, and 49.81 mg/g for SCA1, SCA2, SCA3, and SCA4, respectively; for Cu (II): 24.25, 43.54, 43.35, and 32.42 mg/g for SCA1, SCA2, SCA3, and SCA4, respectively). Moreover, the R^2 values from PSO kinetic equation (R^2 greater than 0.99) were greater than those of the other models. Therefore, the pseudo-second-order kinetic model was more suitable for describing the capture of Pb (II) and Cu (II) by SCA-X, denoting that chemisorption played a predominant part in the adsorption process [45,46]. In addition, three-stage linear components can be

clearly observed in the intraparticle diffusion model, which revealed that multiple steps were involved in the adsorption process. The first stage denoted external diffusion, involving a quick diffusion step of Pb (II) and Cu (II) from the solution to the outer surface of the adsorbent. The second stage belonged to intraparticle diffusion, which showed a lower diffusion rate of Pb (II) and Cu (II) than the first phase. At last, the adsorption sites were gradually reduced and saturated, and the adsorption tended to equilibrate [4]. Thus, intraparticle diffusion model results demonstrated that the adsorption of Pb (II) and Cu (II) depended on multi-steps [47]. The Elovich model was also well suited to experimental data, which suggested that adsorption was a kinetic process governed by the chemical interaction between the SCA-X adsorbents and Pb (II) and Cu (II) [48,49]. Therefore, a chemisorption mechanism was mainly responsible for the adsorption of Pb (II) and Cu (II) based on the above analysis.

3.2.4. Adsorption isotherm

The impact of various concentrations on the adsorption of SCA-X was carried out at 298 K. In **Fig. S6**, SCA-X adsorbents adsorption capacity increased remarkably with increasing metal ion concentration, followed by a plateau. The greater concentration gradient difference between the solid and liquid phases leaded to an increase in mass transfer driving forces as the initial concentration of heavy metal ions increased, the active sites of SCA-X are progressively occupied and eventually the adsorption capacity no longer increased [50]. Clearly, the adsorption capacity of Pb (II) by SCA-X was higher than for Cu (II).

Some models were adopted to elucidate the adsorption mechanism of SCA-X. A fitting curve for adsorption isotherm models can be seen in Fig. 9 and Fig. 10 and its parameters can be found in Table 3. The Langmuir model had higher R^2 values compared to other models, indicating that it can better characterize the adsorption of Cu (II) and Pb (II)
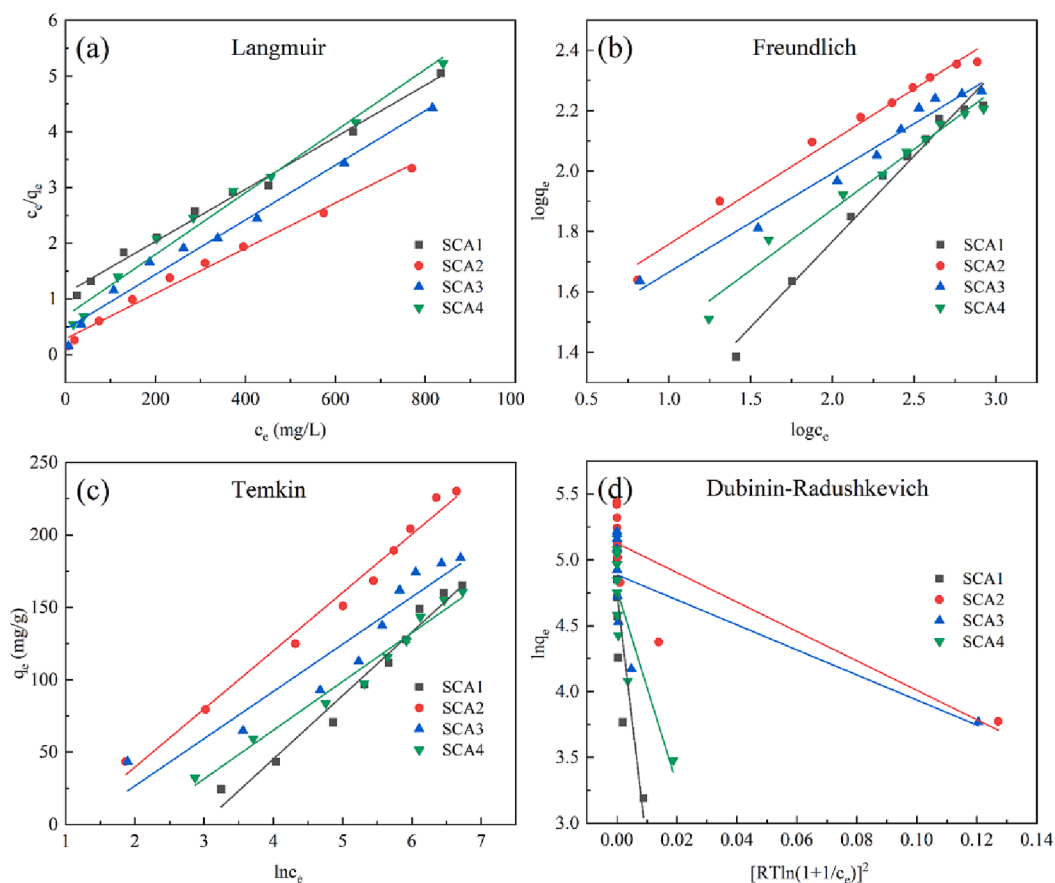
Fig. 10. Adsorption isotherm fitting curve for Cu (II) by SCA-X.

Table 3
Fitting parameters for the adsorption isotherms of Pb (II) and Cu (II) on SCA-X.

Isotherms models	Parameters	Pb (II)				Cu (II)			
		SCA1	SCA2	SCA3	SCA4	SCA1	SCA2	SCA3	SCA4
Langmuir	k_L (L/mg)	0.024	0.041	0.031	0.034	0.004	0.015	0.011	0.008
	q_m (mg/g)	270.27	357.14	322.58	256.41	212.76	243.90	204.08	181.82
	R^2	0.9894	0.9953	0.9904	0.9932	0.9914	0.9899	0.9812	0.9855
Freundlich	k_F ((mg/g)/(mg/L)^n)	56.144	93.132	89.475	79.068	4.285	25.972	21.722	11.746
	n	0.239	0.212	0.192	0.179	0.567	0.343	0.328	0.401
	R^2	0.9865	0.9786	0.9547	0.9440	0.9818	0.9828	0.9785	0.9780
Temkin	k_T (L/g)	4.144	30.634	43.823	41.464	0.051	0.363	0.307	0.127
	B_T	31.075	33.494	28.221	23.570	43.816	40.166	32.607	33.593
	R^2	0.9088	0.9014	0.8691	0.9161	0.9727	0.9851	0.9151	0.9763
Dubinin-Radushkevich	k_{DR} (mol^2/kJ^2)	0.186	0.028	0.031	0.071	191.62	11.17	9.51	73.83
	q_{DR} (mg/g)	189.59	246.73	225.43	199.52	115.29	168.33	132.45	118.20
	E (kJ/mol)	1.636	4.174	4.023	2.654	0.051	0.211	0.229	0.082
	R^2	0.6344	0.6487	0.6769	0.7898	0.7298	0.7190	0.5570	0.7576

and monolayer adsorption occurred on the surface of SCA-X aerogels. The maximum adsorption capacity (q_m) of Pb (II) by Langmuir model was 270.27, 357.14, 322.58, and 256.41 mg/g for SCA1, SCA2, SCA3, SCA4, respectively, with corresponding experimental test values (q_e) of 258.66, 349.73, 309.62, and 251.24 mg/g, respectively. Comparably, the maximum adsorption capacity (q_m) of Cu (II) was 212.76, 243.90, 204.08, and 181.82 mg/g, with experimental test values (q_e) of 165.35, 230.26, 184.28, and 160.78 mg/g, respectively. Furthermore, the calculated separation factors R_L lied in the range of 0 to 1, indicating that the SCA-X adsorbents were favorable for the adsorption process of both Cu (II) and Pb (II) [51]. Besides, the Freundlich model also correlated well (R^2, 0.94–0.98), with K_F [Pb(II)] > K_F [Cu(II)] implying that the SCA-X adsorbent had a greater adsorption potential for Pb (II) than for

Cu (II), which was consistent with the finding of the adsorption experiments [52]. It also indicated that metal ions on SCA-X had a preferential adsorption process due to the Freundlich constant n, which was greater than 0 and less than 1. Additionally, according to the Temkin model (R^2, 0.86–0.98), adsorbent-adsorbate interactions may influence the adsorption process [53]. Table 4 exhibited the comparison of the q_m of SCA-X for Pb (II) and Cu (II) with other reported Schiff base adsorbents in the literature. In comparison with other Schiff base adsorbents, the q_m of SCA-X adsorbent for Pb (II) and Cu (II) in this study were greater than other adsorbents, indicating that SCA-X adsorbent was a promising adsorbent for heavy metals.

Table 4

The maximum adsorption capacity (q_m) of the SCA-X adsorbents compared to other Schiff base adsorbents.

Adsorbents	Ligands	q_m (mg/g)		Reference
		Pb (II)	Cu (II)	
SBA-DSA	bis-salicylaldehyde Schiff base	60.9	36.6	[43]
GOSB	chitosan Schiff base	–	111.11	[38]
Rciaa91	copolymerization chelating Schiff base	296.29	116.29	[54]
PVP-SBA-15	polyvinylpyrrolidone-Aminopropyl Schiff base	175	128	[32]
Cell-Hy	cellulose bearing Chelating Schiff Base	81.32	80.35	[55]
SBA-NPA	pyridyl Schiff base	106.62	48.26	[56]
SCA1	salicylaldehyde silica Schiff base	270.27	212.76	This work
SCA2	salicylaldehyde silica Schiff base	357.14	243.90	This work
SCA3	salicylaldehyde silica Schiff base	322.58	204.08	This work
SCA4	salicylaldehyde silica Schiff base	256.41	181.82	This work

3.2.5. Adsorption thermodynamics

The temperature effect on the absorption of Pb (II) and Cu (II) by SCA-X was studied from 293 to 318 K (Fig. S7). The adsorption of both Pb (II) and Cu (II) by SCA-X adsorbents increased significantly with the increase in temperature, suggesting an endothermic nature of the adsorbent.

Thermodynamics can be used to assess the adsorption reaction and the thermodynamic parameters were shown in Table 5. The plot of lnK_c versus $1/T$ provided the intercept and slope for calculating the ΔS^0 and ΔH^0 parameters (Fig. S8).

ΔG^0 values were negative and became more negative with increasing temperature, demonstrating that the adsorption of Pb (II) and Cu (II) by SCA-X was feasible and thermodynamically spontaneous. All ΔG^0 values for Pb (II) and Cu (II) adsorption by SCA-X varied from 0 to −20 kJ/mol, indicating the involvement of a physical adsorption mechanism within the studied thermo-range [57]. The positive value of ΔH^0 indicated that the adsorption of Pb (II) and Cu (II) on SCA-X was endothermic. All ΔS^0 values were positive, indicating a random increase in the solid/solution interface towards the adsorption of Pb (II) and Cu (II) [58]. In

Table 5

Thermodynamic parameters for the adsorption of Pb (II) and Cu (II) on SCA-X.

Samples	T/K	Pb (II)			Cu (II)		
		ΔG^0/(kJ/mol)	ΔH^0/(kJ/mol)	ΔS^0/(J/(mol·K))	ΔG^0/(kJ/mol)	ΔH^0/(kJ/mol)	ΔS^0/(J/(mol·K))
SCA1	293	−5.627	14.938	70.166	−0.467	13.765	47.019
	298	−5.932			−0.495		
	303	−6.406			−0.595		
	308	−6.576			−0.857		
	313	−7.087			−0.988		
	318	−7.355			−1.067		
SCA2	293	−10.472	18.454	98.804	−3.845	41.101	153.252
	298	−10.970			−4.727		
	303	−11.525			−5.261		
	308	−12.068			−5.683		
	313	−12.354			−6.998		
	318	−12.988			−7.784		
SCA3	293	−11.269	54.076	221.826	−4.116	29.964	115.905
	298	−11.943			−4.644		
	303	−12.749			−4.957		
	308	−14.129			−5.615		
	313	−15.198			−6.197		
	318	−16.856			−7.137		
SCA4	293	−10.724	40.899	176.132	−0.615	15.621	55.344
	298	−11.791			−0.881		
	303	−12.273			−1.190		
	308	−13.173			−1.288		
	313	−14.230			−1.691		
	318	−15.264			−2.054		

Fig. 11. Effect of co-existing ions on the removal of Pb (II) (a) and Cu (II) (b) by SCA2.
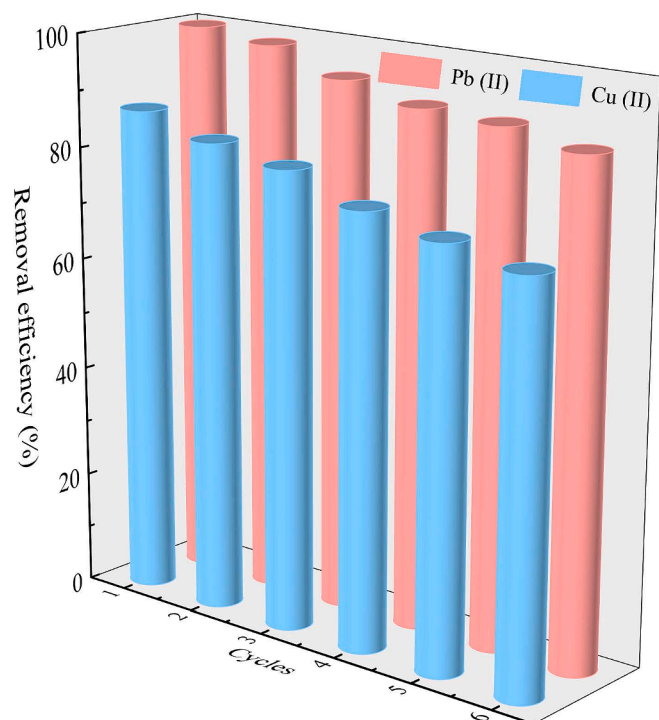
Fig. 12. The reusability of SCA2.

conclusion, SCA-X adsorption of Pb (II) and Cu (II) was essentially a spontaneous endothermic process.

3.2.6. The effect of co-existing ions

There are many types of heavy metal ions in the polluted solutions, such as Hg (II), Zn (II), Cr (III), Cr (VI), which have an impact on the removal of the target ions. Thus, a study was conducted to determine whether co-existing ions affected the removal of Pb (II) and Cu (II) by SCA2. Experiments were performed at 50 mg/L of Pb (II) and Cu (II) solutions under pH 5, mixing with other co-existing ions in the concentration range of 0–50 mg/L, respectively. As can be seen from Fig. 11**a**, the coexisting ions (Hg (II), Zn (II), Cr (III), Cr (VI)) had little effect on the removal of Pb (II). However, when the concentration of co-existing ions was increased to 50 mg/L, the removal of Cu (II) dropped with Hg (II) from 90.87% to 83.09%, with Zn (II) from 90.92% to 86.12%, with Cr (III) from 91.03% to 84.21% and with Cr (VI) from 90.35% to 80.23%. The drop in the removal rate could be related to competing adsorption of heavy metal ions on the active sites (Fig. 11**b**) [59].

3.2.7. Regeneration property

The recovery and reliability of the adsorbents are crucial factors for evaluating its practical application performance. Fig. 12 revealed that the removal efficiency of the SCA2 adsorbent for Pb (II) and Cu (II) reduced with the cycles. After six cycles of recycling, the removal efficiency of the SCA2 adsorbent for Pb (II) and Cu (II) decreased from 99.89% and 87.08% to 88.39% and 71.74%, respectively. The probable reason was incomplete desorption resulting in part of the adsorption sites being occupied [60]. Overall, the recycling experiments proved to be good potential for the reuse of SCA2 adsorbent.

Moreover, to explore the stability of the SCA2, XRD and FTIR spectra of the SCA2 after six cycles of reuse (R-SCA2-Pb and R-SCA2-Cu) was performed. It was found that the amorphous silica peak at around 22° remained in the same position after six cycles of reuse, which confirmed that the cycling operation did not disrupt the skeletal structure of the silica (Fig. S9**a**) [61]. Besides, FTIR spectra after six cycles of reuse showed that the characteristic peaks were maintained after several acid

elution cycles. These results illustrated the high stability of the SCA2 adsorbent (**Fig. S9b**) [62].

3.3. Adsorption mechanism

3.3.1. XPS analysis

XPS analysis coupled with DFT calculations provided in-depth understanding of the adsorption mechanisms of Pb (II) and Cu (II). Fig. 13**a** presented the full spectra of SCA2, SCA2-Pb, and SCA2-Cu. Before the adsorption of Pb (II) and Cu (II), the full spectrum contained four elements C, O, Si, and N. After the adsorption of Pb (II), SCA2-Pb exhibited a new peak at 139 eV corresponding to Pb 4f, and peaks at 412 eV and 435 eV were attributed to Pb 4d5/2 and Pb 4d3/2, respectively [63]. Likewise, there appeared a Cu 2p characteristic peak at 934 eV after the adsorption of Cu (II). These results confirmed that SCA2 was effective in capturing Pb (II) and Cu (II). Fig. 13**b** displayed the high-resolution Pb 4f spectrum with two peaks ascribed to Pb 4f 5/2 (143.85 eV) and Pb 4f 7/2 (138.97 eV) [45,64]. Fig. 13**c** exhibited the Cu 2p double peak corresponding to Cu 2p1/2 (953.48 eV) and Cu 2p3/2 (933.71 eV), respectively [65,66].

Fig. 13**d** illustrated the N 1 s spectrum of SCA2, with splitting into two peaks perceived as C-N (398.69 eV) and C = N (401.01 eV), respectively [67]. After the adsorption of Pb (II), these two peaks of N 1 s can be observed in SCA2-Pb shifting towards 398.95 and 401.79 eV, respectively (Fig. 13**e**). Similarly, the two peaks can be observed to migrate towards 399.65 and 402.96 eV after Cu (II) adsorption in SCA2-Cu (Fig. 13**f**). An increase in binding energy was attributed to the nitrogen atoms electron-sharing with copper and lead, reducing the density of the electron cloud surrounding the nitrogen atom, which suggested that the nitrogen atom participated in the adsorption process [68].

Fig. 13**g** showed the O 1s spectrum of SCA2, which can be split into three peaks at 531.10, 532.36, and 533.73 eV belonging to O-H, Si-O, and C-O, respectively [69,70]. In Fig. 13**(h-i)**, the O 1s peaks of SCA2-Pb belonging to O-H and C-O were shifted from 531.10 and 533.73 eV to 531.23 and 534.01 eV. However, all the O 1s peaks of SCA2-Cu were barely shifted. This demonstrated that the hydroxyl group on the benzene ring of SCA2 was involved in the adsorption of Pb (II) and exhibited little capture of Cu (II). In summary, XPS analysis demonstrated the involvement of Schiff bases and –OH in the adsorption of Pb (II), and only the Schiff bases engaged in the adsorption of Cu (II).

3.3.2. DFT calculation

DFT calculations were performed on the adsorption mechanism of Pb (II) and Cu (II), providing a good illustration of the contribution of various functional groups involved in adsorption. Fig. 14 elucidated the optimization of the SCA2, SCA2-Pb, and SCA2-Cu. E_{ads} less than 0 means beneficial adsorption, whereas E_{ads} more than 0 denotes an unfavorable condition [71]. The calculated adsorption energies revealed that the E_{ads} for Pb (−0.51 eV) was lower than for Cu (-0.42 eV), indicative of Pb (II) being more robust on SCA2 than Cu (II).

Electron donating and electron gaining abilities are expressed in terms of HOMO and LUMO, $E_{gap} = E_{LUMO}\text{-}E_{HOMO}$ is taken as a measurement of how easily a molecule can be excited [72]. Fig. 15 showed the variations of HOMO-LUMO and E_{gap} of SCA2, SCA2-Pb, and SCA2-Cu. Both HOMO and LUMO of SCA2 were observed to be predominantly distributed on the Schiff base group and benzene ring before adsorption. However, a significant change in both HOMO and LUMO was noticed after the adsorption of Pb (II) and Cu (II), revealing the successful adsorption of Pb (II) and Cu (II) onto SCA2. Also, there was a significant fall in the E_{gap} of SCA2-Pb and SCA2-Cu, implying that the adsorption of Pb (II) and Cu (II) destabilized the former steady structure [73].

The adsorption mechanisms of SCA2 interactions with Pb (II) and Cu (II) were further revealed by NBO analysis [74]. The higher the stabilization energy ($E^{(2)}$), the stronger the interaction of the electron-donors
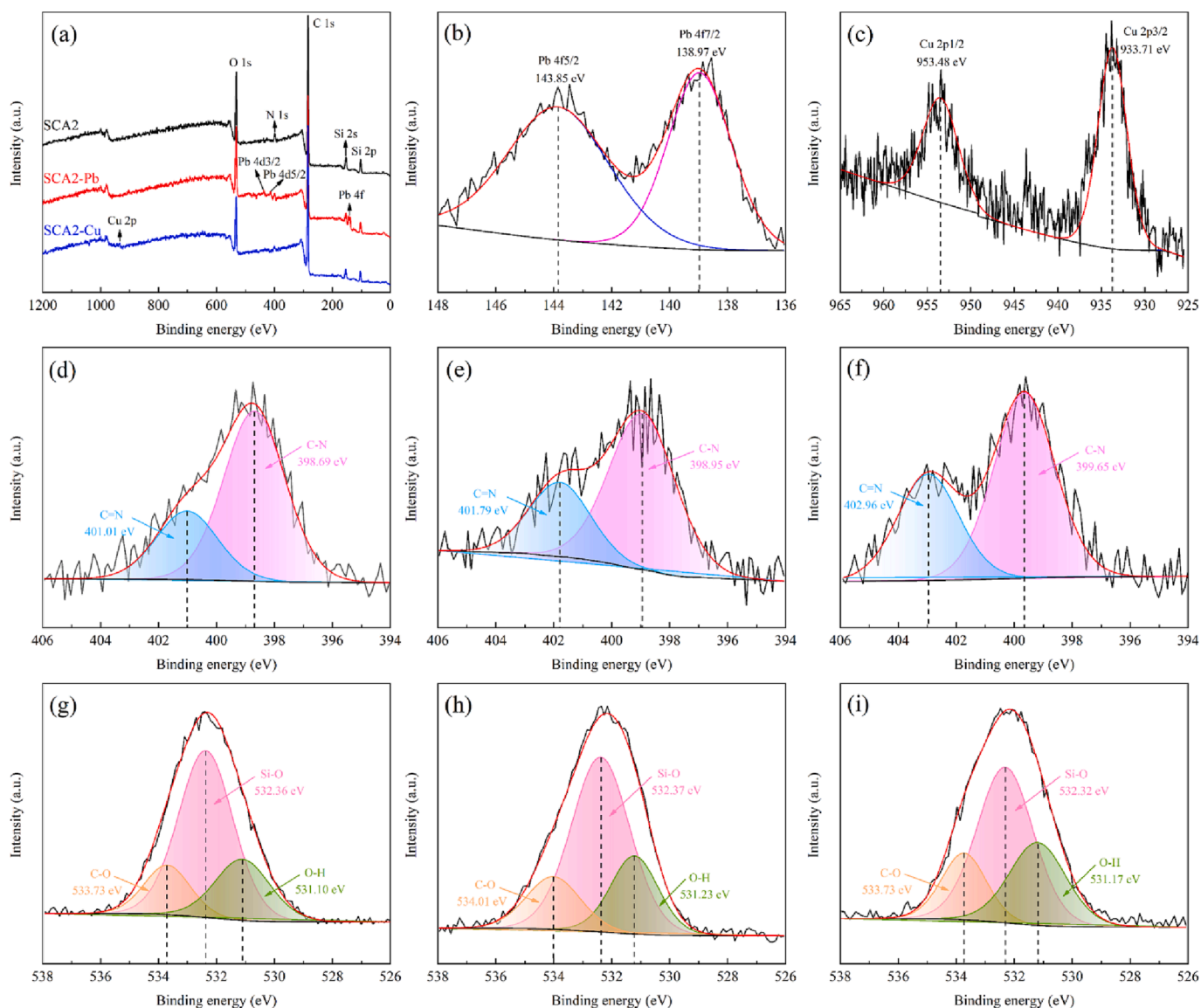
Fig. 13. XPS spectra of SCA2: (a) overall spectrum; (b) high resolution of Pb 4f; (c) high resolution of Cu 2p; N1spectra of SCA2 (d), SCA2-Pb (e) and SCA2-Cu (f); O 1s spectra of SCA2 (g), SCA2-Pb (h) and SCA2-Cu (i).
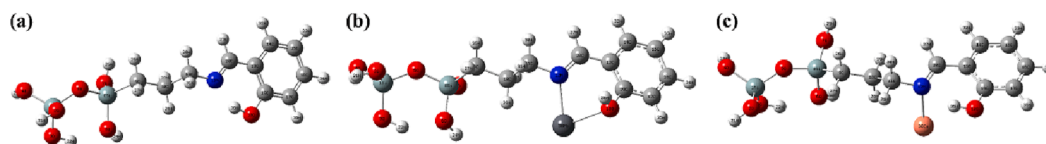
Fig. 14. The optimized geometric model of SCA2 (a), SCA2-Pb (b) andSCA2-Cu (c).

with the electron-acceptors [72]. The main effect of SCA2 interactions with Pb (II) and Cu (II) was controlled by the σ-donation of lone-pair of electrons from the N and O atoms to Pb (II) and Cu (II). As shown in **Table S3**, the $E^{(2)}$ values of LP(N12) → LP*(Pb) and LP(O18) → LP*(Pb) for SCN2-Pb were 8.43 and 4.63 kcal/mol, while the $E^{(2)}$ value of LP (N12) → LP*(Cu) and LP(O18) → LP*(Cu) for SCA2-Cu were 5.36 and 0.07 kcal/mol. A smaller $E^{(2)}$ value for LP(O) → LP*(Pb) than for LP(N) → LP*(Pb) indicated that both N and O atoms of SCA2 were involved in the adsorption of Pb (II) and that the nitrogen atom played a dominant role.

In case of SCA2-Cu, similar results have been found, where the $E^{(2)}$ value for the Schiff base functional group N atoms (LP(N) → LP*(Cu))

was much greater than for LP(O) → LP*(Cu), indicating that the Schiff base functional groups were predominant in the adsorption of Cu (II) [75]. Furthermore, it is clear that the $E^{(2)}$ value for LP(N) → LP*(Pb) was greater than that for LP(N) → LP*(Cu), indicating that SCA2 had a better affinity for Pb (II) than Cu (II) [37]. Thus, DFT calculations have explained the adsorption mechanism of SCA2 for Pb (II) and Cu (II) and unveiled the contribution of different functional groups to the adsorption. In summary, coupled with the above characterization and adsorption performance analysis, it is clear that the predominant role of the SCA2 adsorbent in the adsorption of Pb (II) and Cu (II) was chemisorption, followed by physical adsorption including electrostatic attraction and porous structure [45].
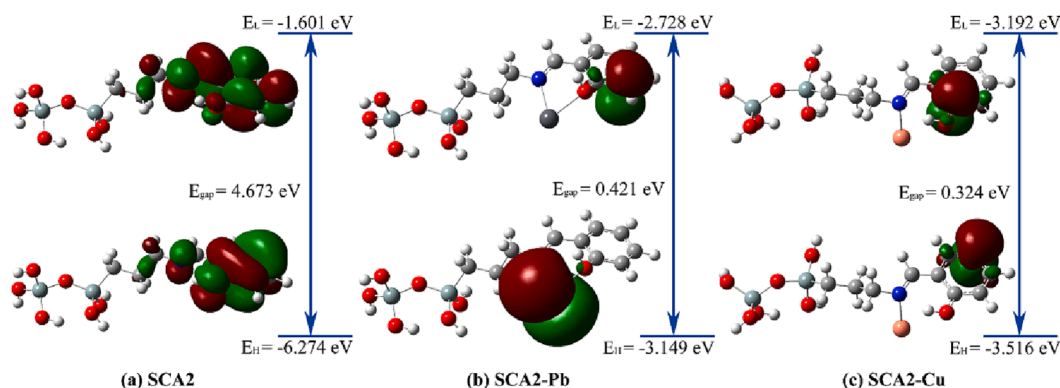
Fig. 15. HOMO and LUMO plots of SCA2 (a), SCA2-Pb (b) and SCA2-Cu (c).

Table 6
Environmental impact of the production of 1 kg SCA2.

Category	Unit	Result
GWP	kg CO$_2$ eq	76.26
AP	kg SO$_2$ eq	0.32
ADP	kg antimony eq	0.01
EP	kg PO$_4^{3-}$eq	0.04
ODP	kg CFC^{-11} eq	1.53E-04
POFP	kg NMVOC eq	0.23
PED	MJ	1618.57

3.4. LCA result

3.4.1. Environmental impacts of SCA2 recommendations for green production

As SCA2 exhibited better properties than other samples (section 3.2), this section applied the LCA method to evaluate the environmental impact of producing 1 kg of SCA2 adsorbent (Table 6). The results indicated that the average values of GWP, AP, ADP, EP, ODP, POFP and PED were 76.26 kg CO$_2$ eq, 0.32 kg SO$_2$ eq, 0.01 kg antimony eq, 0.04 kg PO$_4^{3-}$eq, 1.53E-04 kg CFC^{-11} eq, 0.23 kg NMVOC eq, and 1618.57 MJ respectively. The highest impact was obtained in the PED, i.e. 1618.57 MJ. At the same time the GWP value cannot be ignored, the production of 1 kg of SCA2 generated 76.26 kg CO$_2$ eq. In order to propose a more environmentally friendly and efficient production strategy for SCA2, it is important to analyze the contribution each raw material to the production of adsorbents.

In order to further analyze the environmental impact produced by

the adsorbent during production, the environmental impact categories from all raw materials were normalized to be 100% of all factors for every impact category (Fig. 16). Ethanol accounted for the largest proportion of all materials required for production in most environmental impact categories. It contributed 72.63%, 57.63%, 54.75%, 35.51%, 3.25%, 54.1% and 61.21% to GWP, AP, ADP, EP, ODP, POFP and PED respectively. This is because ethanol acted mainly as a washing and solvent in the preparation of the adsorbent and its high demand leaded to a high proportion of environmental impact. The next factor with a greater environmental impact was n-hexane, which accounted for 9.35%, 17.72%, 39.06%, 28.12%, 3.4%, 39.7% and 26.03% to GWP, AP, ADP, EP, ODP, POFP and PED respectively. The reasons for the high proportion of environmental impact of n-hexane were similar to ethanol. Furthermore, Table 1 indicated that TEOS, APTES and SA were 0.47 kg, 0.35 kg and 0.2 kg respectively, representing around 2.21%, 1.65% and 0.94% of the n-hexane used, but contributing 3.33%, 3.98 and 1.07% to the GWP and 16.07%, 28.12% and 2.96% to the EP of the adsorbent production process. It was worth noting that SA had a significant impact on ODP, accounting for 93% of the impact of all component materials.

3.4.2. Recommendations for green production

The analysis revealed that the five materials mentioned above had a greater impact on the environment during the synthesis of the adsorbents. If one wants to find a method of synthesizing adsorbents with a lower environmental impact, the mechanisms behind the results should be analyzed in order to make recommendations for greener production.

Ethanol and n-hexane are volatile and the main role of both in the production of adsorbents is that of a washing and solvent, and they are
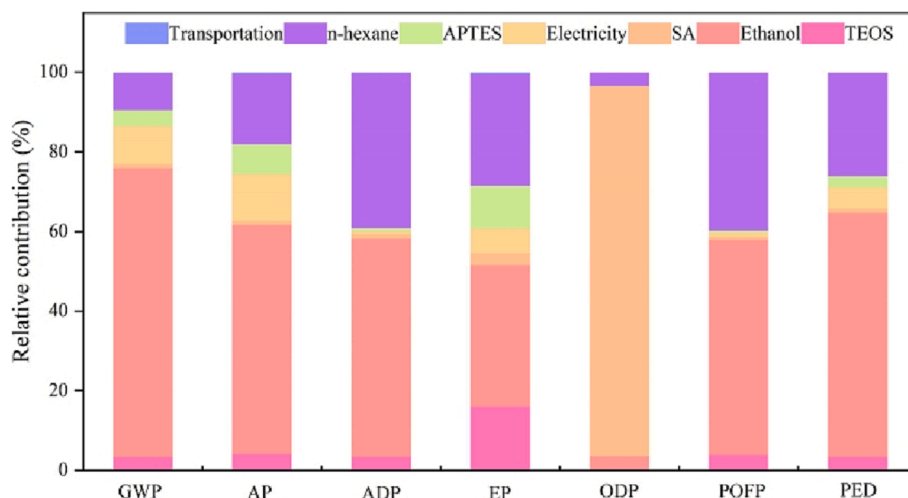

Fig. 16. Relative contribution of environmental impact indicators for SCA2.
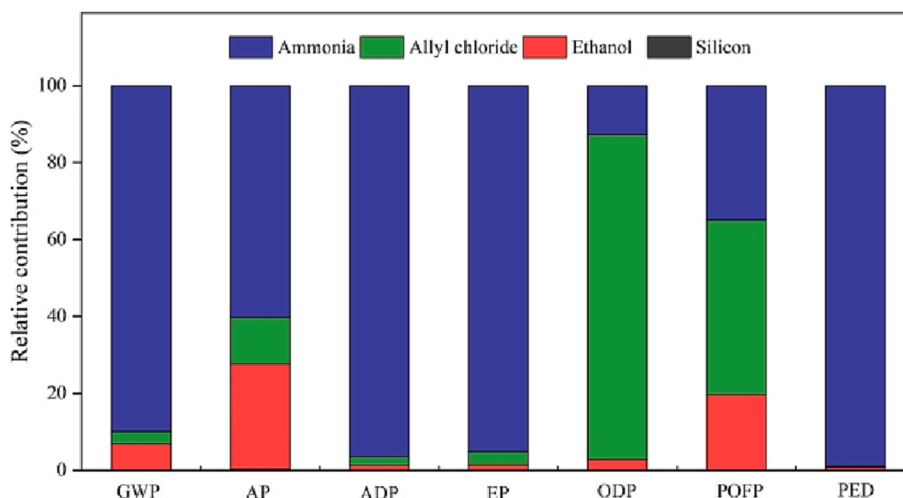
Fig. 17. Relative contribution of environmental impact indicators for APTES.

subject to heat and evaporation during the production process. Therefore, the environmental impact can be greatly reduced by finding a way to collect evaporated ethanol and n-hexane for recovery and recycling.
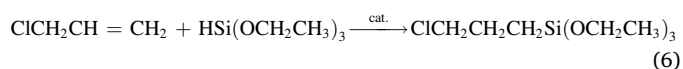
In this work, TEOS is synthesized by alcoholysis of silicon tetrachloride [76]:

$$SiCl_4 + 4ROH \rightarrow Si(OR)_4 + 4HCl \tag{4}$$
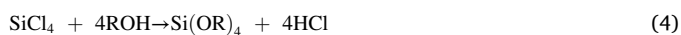
It was found that acidification and established corrosive hydrochloric acid are produced during the production of TEOS. Therefore, it becomes important to explore the role of materials for the synthesis process of TEOS. One typical approach to TEOS replacement is the use of water glass [77]. Water glass is cheaper than TEOS and has not harmful by-products. The classical method of producing water glass is through the reaction between sodium carbonate and silica. As both are salts, they have a low impact on the environment. Although the process of producing water glass by this method requires high temperature conditions and may be accompanied by some greenhouse gas emissions, with the

increased ability to transform wind and solar energy, this will allow a more environmentally friendly way of achieving water glass production conditions. The use of water glass to replace TEOS in the production process is thus positively correlated with the protection of the environment.

Below is the reaction equation of APTES, which can be used to analyze the environmental impact of APTES.

$$Si + CH_3CH_2OH \xrightarrow{cat.} HSi(OCH_2CH_3)_3 + H_2 \tag{5}$$

$$ClCH_2CH = CH_2 + HSi(OCH_2CH_3)_3 \xrightarrow{cat.} ClCH_2CH_2CH_2Si(OCH_2CH_3)_3 \tag{6}$$

$$ClCH_2CH_2CH_2Si(OCH_2CH_3)_3 + NH_3 \xrightarrow{cat.} NH_2CH_2CH_2CH_2Si(OCH_2CH_3)_3 + HCl \tag{7}$$

APTES is produced from allyl chloride, silicon, ethanol, and ammonia working over a catalyst. As the catalyst is not involved in the reaction and can be recycled afterward, its environmental impact is negligible. Fig. 17 showed the results of normalizing the above factors so that all factors in each influence curve are 100%. Ammonia is the largest
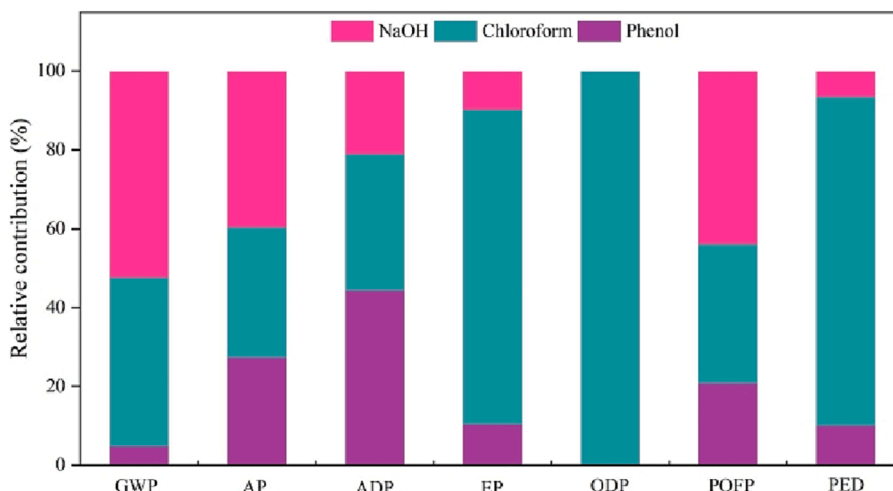

Fig. 18. Relative contribution of environmental impact indicators for SA.

contributor in most environmental categories. The contributions of ammonia to GWP, AP, ADP, EP, ODP, POFP and PED are 89.82%, 60.20%, 96.47%, 95.12%, 12.68%, 34.85% and 98.86% respectively. The ammonia in this study is obtained by the Haber-Bosch process combining hydrogen and nitrogen with iron oxide catalysts at very high pressures and moderate temperatures [78]. Searching for alternatives to ammonia or choosing an environmentally friendly production process could significantly reduce the environmental impact of APTES. Bicer et al. [79] also analyzed ammonia production in different methods and found that the environmental impact of ammonia production using municipal waste incineration plants and hydroelectric methods was significantly less than other methods. Therefore, this idea can also be adapted to produce ammonia in this study, which would result in a noticeably lower environmental impact of APTES.

The synthesis process of SA, which has also been explored in this study, is shown below.

$$(8)$$
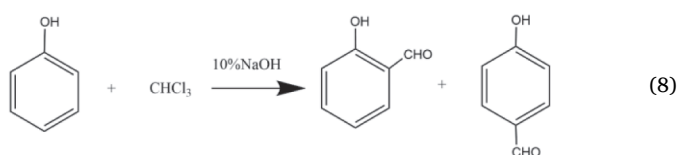
A normalized analysis of the materials used to produce SA. Fig. 18 showed that chloroform and sodium hydroxide have a greater environmental impact. In the ODP environmental category, chloroform has an environmental impact of over 99%. Therefore, finding an environmentally friendly material to replace chloroform in the product process of SA can improve the environment to a greater extent. For sodium hydroxide, a more environmentally friendly product process can be used to reduce its environmental impact.

Furthermore, an assessment was conducted on the cost-effectiveness of the adsorbent gained using atmospheric drying method. The conventional supercritical drying method for the preparation of silica aerogels involves costly, time-consuming, operationally complicated, high-risk, making it difficult to produce on a large scale. Considering the large-scale industrial production of silica aerogels, the atmospheric drying method proved to be an attractive alternative to the supercritical drying process since it is straightforward, cost-effective, short-cycle and safe [80]. Moreover, the LCA environmental impact analysis proposed using water glass as an alternative to TEOS. Kobylinska et al. [81] found that the cost of synthesis using water glass was approximately 10% lower than the method prepared with TEOS, which is both environmentally and economically beneficial in large-scale production. The recycling of ethanol and n-hexane in the solvent exchange process is also a feasible method for large-scale, low-cost production. Therefore, these methods may be regarded as viable preparation options for further large-scale production applications.

4. Conclusions

In this study, a novel Schiff base adsorbent (SCA-X) with excellent adsorption performance for Pb (II) and Cu (II) has been successfully developed using a facile and operational method. The adsorption process was in accordance with the Langmuir isotherm and pseudo-second-order kinetic model, with SCA1, SCA2, SCA3 and SCA4 showing q_m of 270.2 mg/g, 357.1 mg/g, 322.5 mg/g and 256.4 mg/g for Pb (II) and 212.7 mg/g, 243.9 mg/g, 204.0 mg/g and 181.8 mg/g for Cu (II), respectively. The optimum adsorption performance of SCA2 was attributed to the large SSA and the availability of active functional groups. In terms of the adsorption mechanism, the interaction between SCA2 and Pb (II) occurred through the coordination of the nitrogen atom donor in the Schiff base and the oxygen atom donor in the benzene ring with Pb (II) during adsorption, whereas the interaction between SCA2 and Cu (II) occurred mainly through the coordination of the nitrogen atom in the Schiff base with Cu (II). Furthermore, by assessing the

environmental impact of the various materials used in the production of 1 kg of SCA2, an adoptable solution is provided. In conclusion, this study demonstrated the feasibility of a novel and effective heavy metal ion adsorbent, as well as provided a solid basis for sustainable and environmental-friendly SCA2 production, which is crucial for heavy metal wastewater treatment.

Declaration of Competing Interest

The authors declare that they have no known competing financial interests or personal relationships that could have appeared to influence the work reported in this paper.

Data availability

Data will be made available on request.

Acknowledgments

Appendix A. Supplementary data

Supplementary data to this article can be found online at https://doi.org/10.1016/j.cej.2023.142019.

References

[1] M. Vakili, S. Deng, G. Cagnetta, W. Wang, P. Meng, D. Liu, G. Yu, Regeneration of chitosan-based adsorbents used in heavy metal adsorption: a review, Sep. Purif. Technol. 224 (2019) 373–387, https://doi.org/10.1016/j.seppur.2019.05.040.
[2] A. Mojiri, H.A. Aziz, N.Q. Zaman, S.Q. Aziz, M.A. Zahed, Metals removal from municipal landfill leachate and wastewater using adsorbents combined with biological method, Desalin. Water Treat. 57 (6) (2014) 2819–2833, https://doi.org/10.1080/19443994.2014.983180.
[3] S. Mitra, A.J. Chakraborty, A.M. Tareq, T.B. Emran, F. Nainu, A. Khusro, A.M. Idris, M.U. Khandaker, H. Osman, F.A. Alhumaydhi, J. Simal-Gandara, Impact of heavy metals on the environment and human health: novel therapeutic insights to counter the toxicity, J. King Saud Univ. Sci. 34 (3) (2022), 101865, https://doi.org/10.1016/j.jksus.2022.101865.
[4] T. Liu, S. Gou, Y. He, S. Fang, L. Zhou, G. Gou, L. Liu, N-methylene phosphonic chitosan aerogels for efficient capture of Cu^{2+} and Pb^{2+} from aqueous environment, Carbohydr. Polym. 269 (2021), 118355, https://doi.org/10.1016/j.carbpol.2021.118355.
[5] V.V. Dev, K.K. Nair, G. Baburaj, K.A. Krishnan, Pushing the boundaries of heavy metal adsorption: a commentary on strategies to improve adsorption efficiency and modulate process mechanisms, Colloid Interface Sci. Commun. 49 (2022), 100626, https://doi.org/10.1016/j.colcom.2022.100626.
[6] R. Janani, B. Gurunathan, K. Sivakumar, S. Varjani, H.H. Ngo, E. Gnansounou, Advancements in heavy metals removal from effluents employing nano-adsorbents: way towards cleaner production, Environ. Res. 203 (2022) 111815, https://doi.org/10.1016/j.envres.2021.111815.
[7] S. Tighadouini, O. Roby, S. Radi, Z. Lakbaibi, R. Saddik, Y.N. Mabkhot, Z. M. Almarhoon, Y. Garcia, A highly efficient environmental-friendly adsorbent based on Schiff base for removal of Cu(II) from aqueous solutions: a combined experimental and theoretical study, Molecules 26 (17) (2021) 5164, https://doi.org/10.3390/molecules26175164.
[8] N. Alhokbany, T. Ahamad, M. Naushad, S.M. Alshehri, Feasibility of toxic metal removal from aqueous medium using Schiff-base based highly porous nanocomposite: Adsorption characteristics and post characterization, J. Mol. Liq. 294 (2019), 111598, https://doi.org/10.1016/j.molliq.2019.111598.
[9] S. Shahraki, H.S. Delarami, F. Khosravi, Synthesis and characterization of an adsorptive Schiff base-chitosan nanocomposite for removal of Pb(II) ion from aqueous media, Int. J. Biol. Macromol. 139 (2019) 577–586, https://doi.org/10.1016/j.ijbiomac.2019.07.223.
[10] P. Fang, W. Xia, Y. Zhou, Z. Ai, W. Yin, M. Xia, J. Yu, R.-A. Chi, Q. Yue, Ion-imprinted mesoporous silica/magnetic graphene oxide composites functionalized with Schiff-base for selective Cu(II) capture and simultaneously being transformed as a robust heterogeneous catalyst, Chem. Eng. J. 385 (2020) 123847, https://doi.org/10.1016/j.cej.2019.123847.

[11] X. Zhang, J. Ma, B. Zou, L. Ran, L. Zhu, H. Zhang, Z. Ye, L. Zhou, Synthesis of a novel bis Schiff base chelating resin for adsorption of heavy metal ions and catalytic reduction of 4-NP, React. Funct. Polym. 180 (2022), 105409, https://doi.org/10.1016/j.reactfunctpolym.2022.105409.

[12] L. Ren, Z. Yang, L. Huang, Y. He, H. Wang, L. Zhang, Macroscopic poly Schiff base-coated bacteria cellulose with high adsorption performance, Polymers 12 (3) (2020) 714, https://doi.org/10.3390/polym12030714.

[13] R. Ahmad, K. Ansari, M.O. Ejaz, Enhanced sequestration of heavy metals from aqueous solution on polyacrylamide grafted with cell@Fe$_3$O$_4$ nanocomposite, Emergent Mater. 5 (2022) 1517–1531, https://doi.org/10.1007/s42247-021-00338-8.

[14] J. Mittal, R. Ahmad, A. Mariyam, V.K. Gupta, A. Mittal, Expeditious and enhanced sequestration of heavy metal ions from aqueous environment by papaya peel carbon: a green and low cost adsorbent, Desalin. Water Treat. 210 (2021) 365–376, https://doi.org/10.5004/dwt.2021.26562.

[15] I. Hasan, R. Ahmad, A facile synthesis of poly (methyl methacrylate) grafted alginate@cys-bentonite copolymer hybrid nanocomposite for sequestration of heavy metals, Groundw. Sustain. Dev. 8 (2019) 82–92, https://doi.org/10.1016/j.gsd.2018.09.003.

[16] W. Peng, H. Li, Y. Liu, S. Song, A review on heavy metal ions adsorption from water by graphene oxide and its composites, J. Mol. Liq. 230 (2017) 496–504, https://doi.org/10.1016/j.molliq.2017.01.064.

[17] O.A. Oyetade, A.A. Skelton, V.O. Nyamori, S.B. Jonnalagadda, B.S. Martincigh, Experimental and DFT studies on the selective adsorption of Pb^{2+} and Zn^{2+} from aqueous solution by nitrogen-functionalized multiwalled carbon nanotubes, Sep. Purif. Technol. 188 (2017) 174–187, https://doi.org/10.1016/j.seppur.2017.07.022.

[18] C. Qiu, W. Chen, M. Schmidt, F. Majs, T.A. Douglas, T.P. Trainor, Selective adsorption of Pb(II) on an annealed hematite (1102) surface: evidence from crystal truncation rod X-ray diffraction and density functional theory, Environ. Sci. Technol. 54 (11) (2020) 6651–6660, https://doi.org/10.1021/acs.est.0c00060.

[19] L. Xu, Y. Liu, J. Wang, Y. Tang, Z. Zhang, Selective adsorption of Pb^{2+} and Cu^{2+} on amino-modified attapulgite: kinetic, thermal dynamic and DFT studies, J. Hazard. Mater. 404 (Pt A) (2021), 124140, https://doi.org/10.1016/j.jhazmat.2020.124140.

[20] E. Jrc, ILCD Handbook: General Guide for Life Cycle Assessment: Detailed Guidance, Publications Office of the European Union, Luxembourg, 2010.

[21] A. Mirza, R. Ahmad, Novel recyclable (Xanthan gum/montmorillonite) bionanocomposite for the removal of Pb (II) from synthetic and industrial wastewater, Environ. Technol. Innov. 11 (2018) 241–252, https://doi.org/10.1016/j.eti.2018.06.009.

[22] M. Frisch, G.W. Trucks, H.B. Schlegel, G.E. Scuseria, M.A. Robb, J.R. Cheeseman, G. Scalmani, V. Barone, B. Mennucci, G. Petersson, Gaussian 09, revision D. 01, in, Gaussian, Inc., Wallingford CT, (2009).

[23] L. Sellaoui, D.I. Mendoza-Castillo, H.E. Reynel-Ávila, B.A. Ávila-Camacho, L. L. Díaz-Muñoz, H. Ghalla, A. Bonilla-Petriciolet, A.B. Lamine, Understanding the adsorption of Pb^{2+}, Hg^{2+} and Zn^{2+} from aqueous solution on a lignocellulosic biomass char using advanced statistical physics models and density functional theory simulations, Chem. Eng. J. 365 (2019) 305–316, https://doi.org/10.1016/j.cej.2019.02.052.

[24] B. Wang, J. Xuan, X. Yang, Z. Bai, Synergistic DFT-guided design and microfluidic synthesis of high-performance ion-imprinted biosorbents for selective heavy metal removal, Colloids Surf. A Physicochem. Eng. Asp. 626 (2021), 127030, https://doi.org/10.1016/j.colsurfa.2021.127030.

[25] K. Chen, Q. Feng, Y. Feng, D. Ma, D. Wang, Z. Liu, W. Zhu, X. Li, F. Qin, J. Feng, Ultrafast removal of humic acid by amine-modified silica aerogel: Insights from experiments and density functional theory calculation, Chem. Eng. J. 435 (2022), 135171, https://doi.org/10.1016/j.cej.2022.135171.

[26] A. Kazemi, N. Bahramifar, A. Heydari, S.I. Olsen, Life cycle assessment of nanoadsorbents at early stage technological development, J. Clean. Prod. 174 (2018) 527–537, https://doi.org/10.1016/j.jclepro.2017.10.245.

[27] I.O.f. Standardization, Environmental management: life cycle assessment; requirements and guidelines, ISO Geneva, Switzerland, (2006).

[28] M.A. Rajaeifar, A. Akram, B. Ghobadian, S. Rafiee, R. Heijungs, M. Tabatabaei, Environmental impact assessment of olive pomace oil biodiesel production and consumption: a comparative lifecycle assessment, Energy 106 (2016) 87–102, https://doi.org/10.1016/j.energy.2016.03.010.

[29] W. Luo, X. Shu, B. Xu, Z. Liu, Z. Ou, J. Liu, Influence of hydrolysis time on properties of SiO$_2$ aerogels prepared by ambient pressure drying, Arab. J. Sci. Eng. 46 (1) (2020) 477–484, https://doi.org/10.1007/s13369-020-04912-w.

[30] Y. Zhang, Q. Shen, X. Li, H. Xie, C. Nie, Facile synthesis of ternary flexible silica aerogels with coarsened skeleton for oil-water separation, RSC Adv. 10 (69) (2020) 42297–42304, https://doi.org/10.1039/d0ra07906e.

[31] Y. Zhang, L. Magagnin, K. Yuan, Z. Wei, X. Wu, Z. Jiang, W. Wang, Highly-efficient removal of Pb (II) from water by mesoporous amino functionalized silica aerogels: experimental, DFT investigations and Life Cycle Assessment, Micropor. Mesopor. Mater. 345 (2022), 112280, https://doi.org/10.1016/j.micromeso.2022.112280.

[32] M.A. Betiha, Y.M. Moustafa, M.F. El-Shahat, E. Rafik, Polyvinylpyrrolidone-Aminopropyl-SBA-15 schiff Base hybrid for efficient removal of divalent heavy metal cations from wastewater, J. Hazard. Mater. 397 (2020), 122675, https://doi.org/10.1016/j.jhazmat.2020.122675.

[33] J.P. Vareda, P.D. Matos, A.J.M. Valente, L. Durães, C.A. Igwegbe, A new Schiff base organically modified silica aerogel-like material for metal ion adsorption with Ni selectivity, Adsorpt. Sci. Technol. 2022 (2022) 1–18, https://doi.org/10.1155/2022/8237403.

[34] G. Anbarasu, M. Malathy, P. Karthikeyan, R. Rajavel, Silica functionalized Cu(II) acetylacetonate Schiff base complex: an efficient catalyst for the oxidative condensation reaction of benzyl alcohol with amines, J. Solid State Chem. 253 (2017) 305–312, https://doi.org/10.1016/j.jssc.2017.06.012.

[35] Z. Li, S. Zhao, M.M. Koebel, W.J. Malfait, Silica aerogels with tailored chemical functionality, Mater. Des. 193 (2020), 108833, https://doi.org/10.1016/j.matdes.2020.108833.

[36] N. Yao, S. Cao, K.L. Yeung, Mesoporous TiO$_2$–SiO$_2$ aerogels with hierarchal pore structures, Micropor. Mesopor. Mater. 117 (3) (2009) 570–579, https://doi.org/10.1016/j.micromeso.2008.08.020.

[37] Y. Zhou, L. Luan, B. Tang, Y. Niu, R. Qu, Y. Liu, W. Xu, Fabrication of Schiff base decorated PAMAM dendrimer/magnetic Fe$_3$O$_4$ for selective removal of aqueous Hg (II), Chem. Eng. J. 398 (2020), 125651, https://doi.org/10.1016/j.cej.2020.125651.

[38] S.M. Anush, H.R. Chandan, B. Vishalakshi, Synthesis and metal ion adsorption characteristics of graphene oxide incorporated chitosan Schiff base, Int. J. Biol. Macromol. 126 (2019) 908–916, https://doi.org/10.1016/j.ijbiomac.2018.12.164.

[39] C. Lei, F. Wen, J. Chen, W. Chen, Y. Huang, B. Wang, Mussel-inspired synthesis of magnetic carboxymethyl chitosan aerogel for removal cationic and anionic dyes from aqueous solution, Polymer 213 (2021) 123316, https://doi.org/10.1016/j.polymer.2020.123316.

[40] Y. Song, S. Wang, L.-Y. Yang, D. Yu, Y.-G. Wang, X.-K. Ouyang, Facile fabrication of core–shell/bead-like ethylenediamine-functionalized Al-pillared montmorillonite/calcium alginate for As (V) ion adsorption, Int. J. Biol. Macromol. 131 (2019) 971–979, https://doi.org/10.1016/j.ijbiomac.2019.03.172.

[41] L. Luan, B. Tang, S. Ma, L. Sun, W. Xu, A. Wang, Y. Niu, Removal of aqueous Zn(II) and Ni(II) by Schiff base functionalized PAMAM dendrimer/silica hybrid materials, J. Mol. Liq. 330 (2021), 115634, https://doi.org/10.1016/j.molliq.2021.115634.

[42] X. Zeng, G. Zhang, Z. Wu, Preparation and characterization of Schiff-base modified Fe$_3$O$_4$ hybrid material and its selective adsorption for aqueous Hg^{2+}, Environ. Sci. Pollut. Res. Int. 29 (20) (2022) 30324–30336, https://doi.org/10.1007/s11356-021-17949-7.

[43] Y. Zhang, G. Wu, Y. Yang, J. Sun, D. Zhang, Preparation of SBA-15 mesoporous silica grafted with bis-salicylaldehyde Schiff base for uptake of Pb(II) and Cu(II) from water, J. Sol-Gel Sci. Technol. 98 (1) (2021) 170–182, https://doi.org/10.1007/s10971-020-05455-0.

[44] Z.-H. Hu, A.M. Omer, X.-K. Ouyang, D. Yu, Fabrication of carboxylated cellulose nanocrystal/sodium alginate hydrogel beads for adsorption of Pb(II) from aqueous solution, Int. J. Biol. Macromol. 108 (2018) 149–157, https://doi.org/10.1016/j.ijbiomac.2017.11.171.

[45] J. Shen, X. Xu, X.-K. Ouyang, M.-C. Jin, Adsorption of Pb (II) from aqueous solutions using nanocrystalline cellulose/sodium alginate/K-Carrageenan composite hydrogel beads, J. Polym. Environ. 30 (2022) 1995–2006, https://doi.org/10.1007/s10924-021-02334-9.

[46] Y. Gao, R.Y. Zhou, L. Yao, W. Yin, J.X. Yu, Q. Yue, Z. Xue, H. He, B. Gao, Synthesis of rice husk-based ion-imprinted polymer for selective capturing Cu(II) from aqueous solution and re-use of its waste material in Glaser coupling reaction, J. Hazard. Mater. 424 (Pt A) (2022), 127203, https://doi.org/10.1016/j.jhazmat.2021.127203.

[47] N. Maaloul, P. Oulego, M. Rendueles, A. Ghorbal, M. Díaz, Biopolymer composite from cellulose nanocrystals of almond (Prunus dulcis) shell as effective adsorbents for Cu^{2+} ions from aqueous solutions, J. Environ. Chem. 9 (2) (2021), 105139, https://doi.org/10.1016/j.jece.2021.105139.

[48] H. Azad, M. Mohsennia, C. Cheng, A. Amini, Facile fabrication of PVB-PVA blend polymer nanocomposite for simultaneous removal of heavy metal ions from aqueous solutions: kinetic, equilibrium, reusability and adsorption mechanism, J. Environ. Chem. 9 (5) (2021), 106214, https://doi.org/10.1016/j.jece.2021.106214.

[49] T.S. Machado, L. Crestani, G. Marchezi, F. Melara, J.R. de Mello, G.L. Dotto, J. S. Piccin, Synthesis of glutaraldehyde-modified silica/chitosan composites for the removal of water-soluble diclofenac sodium, Carbohydr. Polym. 277 (2022), 118868, https://doi.org/10.1016/j.carbpol.2021.118868.

[50] Y. He, S. Gou, L. Zhou, L. Tang, T. Liu, L. Liu, M. Duan, Amidoxime-functionalized polyacrylamide-modified chitosan containing imidazoline groups for effective removal of Cu^{2+} and Ni^{2+}, Carbohydr. Polym. 252 (2021), 117160 https://doi.org/10.1016/j.carbpol.2020.117160.

[51] Y. Yang, L. Zeng, Z. Lin, H. Jiang, A. Zhang, Adsorption of Pb^{2+}, Cu^{2+} and Cd^{2+} by sulfhydryl modified chitosan beads, Carbohydr. Polym. 274 (2021), 118622, https://doi.org/10.1016/j.carbpol.2021.118622.

[52] Y. Yue, Y. Liu, W. Zhang, J. Guo, Y. Gong, Y. Yu, Amidoxime functionalized low-cost cellulose-based adsorbent derived from waste cigarette filters for efficient heavy metal removal, J. Environ. Chem. Eng. 10 (3) (2022), 107846, https://doi.org/10.1016/j.jece.2022.107846.

[53] H. Chen, Y. Gao, A. El-Naggar, N.K. Niazi, C. Sun, S.M. Shaheen, D. Hou, X. Yang, Z. Tang, Z. Liu, H. Hou, W. Chen, J. Rinklebe, M. Pohorely, H. Wang, Enhanced sorption of trivalent antimony by chitosan-loaded biochar in aqueous solutions: characterization, performance and mechanisms, J. Hazard. Mater. 425 (2022), 127971, https://doi.org/10.1016/j.jhazmat.2021.127971.

[54] F.A. Al-Yusufy, M.Q. Al-Qadasy, Y.M.S. Jamil, H.M. Al-Maydama, M.M. Akeel, A comparative study of Schiff base chelating resins: synthesis, uptake of heavy metal ions, and thermal studies, Ecléctica Quím. J. 43 (2) (2018) 10–22, https://doi.org/10.26850/1678-4618eqj.v43.2.2018.p10-22.

[55] R. Saravanan, L. Ravikumar, Renewable modified cellulose bearing chelating Schiff base for adsorptive removal of heavy metal ions and antibacterial action, Water Environ. Res. 89 (7) (2017) 629–640, https://doi.org/10.2175/106143016X14733681696329.

[56] Y. Zhang, X. Cao, J. Sun, G. Wu, J. Wang, D. Zhang, Synthesis of pyridyl Schiff base functionalized SBA-15 mesoporous silica for the removal of Cu(II) and Pb(II) from aqueous solution, J. Sol-Gel Sci. Technol. 94 (3) (2019) 658–670, https://doi.org/10.1007/s10971-019-05205-x.

[57] S. Yadav, A. Asthana, A.K. Singh, R. Chakraborty, S.S. Vidya, M. Susan, S.A. C. Carabineiro, Adsorption of cationic dyes, drugs and metal from aqueous solutions using a polymer composite of magnetic/beta-cyclodextrin/activated charcoal/Na alginate: isotherm, kinetics and regeneration studies, J. Hazard. Mater. 409 (2021), 124840, https://doi.org/10.1016/j.jhazmat.2020.124840.

[58] T. Shi, Z. Xie, Z. Zhu, W. Shi, Y. Liu, M. Liu, Highly efficient and selective adsorption of heavy metal ions by hydrazide-modified sodium alginate, Carbohydr. Polym. 276 (2022), 118797, https://doi.org/10.1016/j.carbpol.2021.118797.

[59] M. Mahmud, M.S. Hossain, M.B. Mobarak, M.S. Quddus, M.S. Bashar, U.S. Akhtar, S.A. Jahan, D. Islam, S. Ahmed, Engineering GO@Zn–Hap@CA porous heterostructure for ultra-fast and ultra-high adsorption efficacy: investigation towards the remediation of chromium and lead, Environ. Sci. Adv. 1 (5) (2022) 827–848, https://doi.org/10.1039/d2va00142j.

[60] H. Zhao, X.-K. Ouyang, L.-Y. Yang, Adsorption of lead ions from aqueous solutions by porous cellulose nanofiber–sodium alginate hydrogel beads, J. Mol. Liq. 324 (2021), 115122, https://doi.org/10.1016/j.molliq.2020.115122.

[61] W. He, Q. Yu, N. Wang, X.-K. Ouyang, Efficient adsorption of Cu (II) from aqueous solutions by acid-resistant and recyclable ethylenediamine tetraacetic acid-grafted polyvinyl alcohol/chitosan beads, J. Mol. Liq. 316 (2020), 113856, https://doi.org/10.1016/j.molliq.2020.113856.

[62] D. Hu, Z. Lian, H. Xian, R. Jiang, N. Wang, Y. Weng, X. Peng, S. Wang, X.-K. Ouyang, Adsorption of Pb (II) from aqueous solution by polyacrylic acid grafted magnetic chitosan nanocomposite, Int. J. Biol. Macromol. 154 (2020) 1537–1547, https://doi.org/10.1016/j.ijbiomac.2019.11.038.

[63] H. Wang, Q. Gao, H. Li, G. Wang, B. Han, K. Xia, C. Zhou, Hydrous titania nanosheets constructed hierarchical hollow microspheres as a highly efficient dual-use decontaminant for elimination of heavy metal ions and organic pollutants, Chem. Eng. J. 381 (2020) 122638, https://doi.org/10.1016/j.cej.2019.122638.

[64] L. Hou, G. Qin, Y. Qu, C. Yang, X. Rao, Y. Gao, X. Zhu, Fabrication of recoverable magnetic composite material based on graphene oxide for fast removal of lead and cadmium ions from aqueous solution, J. Chem. Technol. Biotechnol. 96 (5) (2021) 1345–1357, https://doi.org/10.1002/jctb.6655.

[65] H. Zhang, A.M. Omer, Z. Hu, L.-Y. Yang, C. Ji, X.-K. Ouyang, Fabrication of magnetic bentonite/carboxymethyl chitosan/sodium alginate hydrogel beads for Cu (II) adsorption, Int. J. Biol. Macromol. 135 (2019) 490–500, https://doi.org/10.1016/j.ijbiomac.2019.05.185.

[66] Y. Zhang, X. Cao, L. Zhen, X. Wang, A mesoporous silica-based fluorescent chemosensor bearing bis-Schiff base for the sensitive detection of Cu^{2+} ions, J. Solid State Chem. 297 (2021), 122093, https://doi.org/10.1016/j.jssc.2021.122093.

[67] H. Ebrahimiasl, D. Azarifar, Copper-based Schiff base complex immobilized on core-shell Fe_3O_4@SiO_2 as a magnetically recyclable and highly efficient nanocatalyst for green synthesis of 2-amino-4H-chromene derivatives, Appl. Organomet. Chem. 34 (3) (2019) 5359, https://doi.org/10.1002/aoc.5359.

[68] L. Zheng, Y. Yang, Y. Zhang, T. Zhu, X. Wang, Functionalization of SBA-15 mesoporous silica with bis-schiff base for the selective removal of Pb(II) from water, J. Solid State Chem. 301 (2021), 122320, https://doi.org/10.1016/j.jssc.2021.122320.

[69] N. Pan, L. Li, J. Ding, R. Wang, Y. Jin, C. Xia, A Schiff base/quaternary ammonium salt bifunctional graphene oxide as an efficient adsorbent for removal of Th(IV)/U (VI), J. Colloid Interface Sci. 508 (2017) 303–312, https://doi.org/10.1016/j.jcis.2017.08.068.

[70] C. Ren, X. Ding, H. Fu, C. Meng, W. Li, H. Yang, Preparation of amino-functionalized $CoFe_2O_4$@SiO_2 magnetic nanocomposites for potential application in absorbing heavy metal ions, RSC Adv. 6 (76) (2016) 72479–72486, https://doi.org/10.1039/c6ra13304e.

[71] C. Ji, M. Xu, H. Yu, L. Lv, W. Zhang, Mechanistic insight into selective adsorption and easy regeneration of carboxyl-functionalized MOFs towards heavy metals, J. Hazard. Mater. 424 (Pt D) (2022), 127684, https://doi.org/10.1016/j.jhazmat.2021.127684.

[72] M. Rezaei-Sameti, P. Zarei, NBO, AIM, HOMO–LUMO and thermodynamic investigation of the nitrate ion adsorption on the surface of pristine, Al and Ga doped BNNTs: a DFT study, Adsorption 24 (8) (2018) 757–767, https://doi.org/10.1007/s10450-018-9977-7.

[73] J. Zhang, T. Li, X. Li, Y. Liu, N. Li, Y. Wang, X. Li, A key role of inner-cation-pi interaction in adsorption of Pb(II) on carbon nanotubes: experimental and DFT studies, J. Hazard. Mater. 412 (2021), 125187, https://doi.org/10.1016/j.jhazmat.2021.125187.

[74] Y. Niu, S. Zhao, G. Chen, R. Qu, C. Zhou, L. Wang, S. Feng, Combined theoretical and experimental study on the adsorption mechanism of poly(4-vinylbenzyl 2-hydroxyethyl) sulfide, sulfoxide, and sulfone for Hg(II) and Pb(II), J. Mol. Liq. 219 (2016) 1065–1070, https://doi.org/10.1016/j.molliq.2016.04.043.

[75] X. Song, Y. Niu, P. Zhang, C. Zhang, Z. Zhang, Y. Zhu, R. Qu, Removal of Co(II) from fuel ethanol by silica-gel supported PAMAM dendrimers: combined experimental and theoretical study, Fuel 199 (2017) 91–101, https://doi.org/10.1016/j.fuel.2017.02.076.

[76] S.S. Chadwick, Ullmann's encyclopedia of industrial chemistry, Ref. Services Rev. 16 (1988) 31–34, https://doi.org/10.1108/eb049034.

[77] Y. Guo, H. Wang, L. Zeng, SiO_2 aerogels prepared by ambient pressure drying with ternary azeotropes as components of pore fluid, J. Non-Cryst. Solids 428 (2015) 1–5, https://doi.org/10.1016/j.jnoncrysol.2015.07.030.

[78] M.E. Gálvez, M. Halmann, A. Steinfeld, Ammonia production via a two-step Al_2O_3/AlN thermochemical cycle. 1. Thermodynamic, environmental, and economic analyses, Ind. Eng. Chem. Res. 46 (2007) 2042–2046, https://doi.org/10.1021/ie061550u.

[79] Y. Bicer, I. Dincer, C. Zamfirescu, G. Vezina, F. Raso, Comparative life cycle assessment of various ammonia production methods, J. Clean. Prod. 135 (2016) 1379–1395, https://doi.org/10.1016/j.jclepro.2016.07.023.

[80] W. Luo, X. Shu, B. Xu, Z. Liu, Z. Ou, J. Liu, Influence of hydrolysis time on properties of SiO_2 aerogels prepared by ambient pressure drying, Arab. J. Sci. Eng. 46 (2021) 477–484, https://doi.org/10.1007/s13369-020-04912-w.

[81] N.G. Kobylinska, V.G. Kessler, G.A. Seisenbaeva, O.A. Dudarko, In situ functionalized mesoporous silicas for sustainable remediation strategies in removal of inorganic pollutants from contaminated environmental water, ACS Omega 7 (27) (2022) 23576–23590. http://pubs.acs.org/journal/acsodf.